

**University of Alberta**

The Cooling of The Neutron Star In The Cassiopeia A Supernova Remnant

by

**Khaled Elshamouty**

A thesis submitted to the Faculty of Graduate Studies and Research  
in partial fulfillment of the requirements for the degree of

**Master of Science**

**Department of Physics**

©Khaled Elshamouty  
Fall 2012  
Edmonton, Alberta

Permission is hereby granted to the University of Alberta Libraries to reproduce single copies of this thesis and to lend or sell such copies for private, scholarly or scientific research purposes only. Where the thesis is converted to, or otherwise made available in digital form, the University of Alberta will advise potential users of the thesis of these terms.

The author reserves all other publication and other rights in association with the copyright in the thesis and, except as herein before provided, neither the thesis nor any substantial portion thereof may be printed or otherwise reproduced in any material form whatsoever without the author's prior written permission.

*To my grandmother, you are always here*

---

## ABSTRACT

---

A young neutron star cools mainly via neutrino emission from the star's core. Thus, the thermal evolution of neutron stars reflects changes in their core, constraining temperature-sensitive properties such as the composition of the core and the envelope of the neutron star. The neutron star in the Cassiopeia A supernova remnant (Cas A NS) is the youngest known, at only 330 years old. [Heinke and Ho](#) reported a drop of 3.6% in its surface temperature (21% drop in observed flux) from Chandra ACIS-S X-ray data on the Cas A NS between 2000 and 2009. This is the only young neutron star to have been observed to cool over time, permitting a clearer picture of its thermal evolution. This drop was interpreted as enhanced neutrino emission due to a superfluid transition in the core [\[40\]](#), [\[58\]](#).

Here I present analysis of data from another Chandra detector (HRC-S) over the same time period to test the cooling rate. I used the best current estimates of the effective area of this detector and the spectrum of the Cas A NS to infer the countrates corresponding to various NS temperatures, and thus to compute the temperature drop from the countrate change. The temperature drop inferred from HRC-S observations is more uncertain, but is significantly less than the temperature drop inferred from ACIS-S. Observations using Chandra's other detectors suffer a variety of systematic uncertainties. The result suggests that the temperature drop could be half as large as originally suggested, but that the Cas A NS's temperature is indeed decreasing.

*The hardest arithmetic to master is that which enables us to count our blessings.*

— Eric Hoffer

---

## ACKNOWLEDGMENTS

---

Foremost, my sincerest gratitude to my supervisor **Craig Heinke** for all the support, effort and time he gave to patiently help me despite my continuous bugging through this work. I attribute what I have learned to the continuous tutoring he provided, which was more than valuable. This work would not have been possible without him. He has been a friendly supervisor more than one could wish. Continuous discussions and suggestions on improving the work method from **Gregory Sivakoff** were extremely beneficial. I thank him for this great help. The environment presented in the **Physics Department** at University of Alberta was great for keeping my enthusiasm high, enabling me to do better work. I also thank everyone who made my way to graduate school possible, **Craig Markwardt** and **Randall Smith**, I hope I did not let them down. My previous supervisor, **Aladdin Abdul-latif** who taught me the importance of seeing and feeling the science of everything.

I can not thank my parents **Gamal Elshamouty**, **Nagwa Shahbou** and my larger **family** enough for every kind of support they provided, and are providing, me in every step. I find no fair words to thank them enough.

I am deeply grateful to **Mahmoud Mohsen**, **Amira Gamea**, **Ahmed Nabil** and **Mai Elkatatny** for always believing in me and pushing me do better. Their moral support imprinted a great value of confidence and encouragement that shall be forever remembered.

---

## CONTENTS

---

1	INTRODUCTION - <i>the what?</i>	1
1.1	Life Story	1
1.2	Supernova	2
1.3	Formation of Neutron Stars	3
1.4	The Cooling of Neutron Stars	6
2	<i>Chandra</i> X-RAY OBSERVATORY - <i>the how?</i>	9
2.1	X-ray Astronomy	9
2.2	Chandra X-Ray Observatory	10
2.3	High Resolution Mirror Assembly (HRMA)	10
2.3.1	Advanced CCD Imaging Spectrometer (ACIS)	11
2.3.2	High Resolution Camera (HRC)	14
3	CASSIOPEIA A - <i>the why?</i>	17
3.1	The Supernova Remnant	17
3.2	Central Compact Object	18
3.3	The mystery of a carbon atmosphere	21
3.4	Detection of Cooling	22
3.5	Physical Interpretation	23
4	TESTING THE COOLING - <i>the now what?</i>	28
4.1	Rationale	28
4.2	Methods	29
4.2.1	HRC-S:	30
4.2.2	HRC-I:	32
4.2.3	ACIS-I:	33
4.2.4	ACIS-S, FAINT Mode	38
4.3	Results and Discussion	38
4.3.1	HRC-S:	38
4.3.2	Other detectors:	43
4.4	Conclusion	45
	BIBLIOGRAPHY	48

---

## LIST OF TABLES

---

Table 4.1	The derived HRC-I temperatures from the best fit values of the non-magnetized Carbon atmosphere ACIS-S spectrum. The best fit for the drop is $8.9 \pm -1.7\%$ over 10 years with very poor $\chi^2 = 40$ for 17 d.o.f. 34
Table 4.2	The derived ACIS-I temperatures from the best fit values of the non-magnetized Carbon atmosphere ACIS-S spectrum. The best fit for the drop is $8.9 \pm -1.7\%$ over 10 years, with very poor $\chi^2 = 60$ for 21 d.o.f. 37
Table 4.3	The derived ACIS-S (FAINT) temperatures from the best fit values of the non-magnetized Carbon atmosphere ACIS-S spectrum. The best fit for the drop in temperature is $8.9 \pm -1.7\%$ over 10 years, with very poor $\chi^2 = 9.3$ for 16 d.o.f. 39
Table 4.4	The inferred HRC-S temperatures computed from the countrates, using appropriate responses and assuming a simulated carbon atmosphere spectrum, for different choices of source and background region. The radii of the different cases are: <b>Case I:</b> Source= 1.3", background= 2"-3.3", <b>Case II:</b> Source= 1.97", background= 2.5"- 3.9", <b>Case III:</b> Source= 3", background= 5"- 8" and <b>Case IV:</b> Source= 3", background= 5"- 8" with filaments in <a href="#">Figure 4.3</a> excluded. 42

---

## LIST OF FIGURES

---

- Figure 2.1 The Advanced CCD Imaging Spectrometer (ACIS) detector on *Chandra*. It has two detectors; ACIS-I optimized for imaging and ACIS-S optimized for spectroscopy. ACIS can be used with the High Energy Transmission grating to give high spectral resolution. The aim-points are marked with ( $\times$ ). Figure from (<http://cxc.harvard.edu/cal/Acis/>) 11
- Figure 2.2 The combined effective area of HRMA/ACIS at different energies. Figure from (<http://cxc.harvard.edu/proposer/POG/html/chap6.html>). 14
- Figure 2.3 The High Resolution Camera (HRC) microchannel plates (MCP) offer the highest spatial resolution (0.4"). The HRC consists of two detectors, HRC-I, which is optimized for imaging and HRC-S, which is optimized for high-resolution spectroscopy when used with the Low Energy Transmission Grating (LETG). Figure from (<http://cxc.harvard.edu/cal/Hrc/index.html>) 15
- Figure 3.1 Superfluid energy gap  $\Delta$  versus different densities for the  $^1S_0$  and  $^3P_2$  configurations. At lower densities (e.g. the inner crust) the superfluid are paired up at  $^1S_0$  with higher energy gap. As the density increases in the core ( $> 10^{14}$  g cm $^{-3}$ ) superfluid neutrons are paired up in  $^3P_2$  configuration. Figure from [53]. 24
- Figure 3.2 The theoretical different cooling curves of a  $1.4 M_{\odot}$  neutron star as a function of time using APR equation of state with envelope of heavy elements. The comparison shows the effect of the nucleon pairing and the the continuous breaking and formation process (PBF) on the cooling curves. The cooling is steeper when nucleon pairing is present along with the PBF process being turned on. Figure from [39]. 25

- Figure 3.3 The different theoretical cooling curves as a function of time.  $T_2^\infty$  is the redshifted effective temperature of the neutron star. This figure shows that the cooling curves are strongly dependent on the superfluid critical temperature  $T_C$  for the  ${}^3P_2$  neutrons (in units of  $(10^9 \text{ K})$ ). The neutron star is assumed to be thermally relaxed and the core is isothermal. Figure from [40]. 26
- Figure 4.1 Comparison between two deep ACIS-S observations for the neutron star in Cas A. **Left:** ObsID 10935 in 2009 with exposure of 25 ks, showing strong filamentary structure in the vicinity of the neutron star. **Right:** ObsID 114 taken in 2000 with a 50 ks exposure, shows that these filaments were less bright. The simplest assumption is that the filamentary structure crosses the neutron star as well as the background. It is very difficult to reach to a robust conclusion about the exact behaviour of these filaments. 32
- Figure 4.2 HRMA/HRC-I point spread function (PSF) as a function of energy enclosed for on-axis observations. The red vertical line corresponds to the 1.3" radius of the source region considered in the analysis to ensure a minimum  $\sim 90\%$  of the source energy at 1.5 keV is enclosed. Source: Chandra X-ray Observatory Proposer's Guide. 33
- Figure 4.3 **Dashed line** regions represents the background considered. The two ellipses are the excluded regions with the filament activity. Annulus is 5"-8" and the **solid line** region is the source with radius of 3". 2009 HRC-S ObsID 10227 image of Cas A NS. 35
- Figure 4.4 ObsID 9698 is shown. **Solid line** region is the source with 4.2" radius. **Dashed line** region is the background region. The red dashed line is excluded region from background. These regions are the fixed for all ACIS-I analysis. 36
- Figure 4.5 Histogram of the number of observations at different off-axis angles (in arcmin) using ACIS-I detector. 36
- Figure 4.6 The smearing of the image of the neutron star in ACIS-I ObsID 2876 as a result of its 5.4' off-axis angle. 38

- Figure 4.7 Inferred temperatures ( $1 - \sigma$ ) from HRC-S countrates, assuming the carbon atmosphere model spectrum, using a large background (b) annulus. Different choices of source size (s), and choices of whether regions containing bright supernova remnant filaments are removed from the background annulus, are compared. Different choices of source region produce a larger countrate variation than whether bright filaments are excluded from the background annulus. 40
- Figure 4.8 Inferred temperatures ( $1 - \sigma$ ) from HRC-S countrates, assuming the carbon atmosphere model spectrum, with different choices of source (s) and background (b) extraction regions. The temperature drop ranges from  $0.9^{+0.6\%}_{-0.6\%} - 1.9^{+0.7\%}_{-0.7\%}$  within  $1 - \sigma$  level with  $\chi^2=8.3$  for 6 d.o.f 41
- Figure 4.9 The measured temperatures ( $1 - \sigma$ ) from ACIS-I for the neutron star in Cas A, assuming the carbon atmosphere model spectrum. Linear fitting indicates a decline of  $8.9^{+1.7\%}_{-1.7\%}$  over 10 years (with  $1 - \sigma$  errors). The linear fit is poor with a  $\chi^2$  of 60 for 21 degrees of freedom. 44
- Figure 4.10 Inferred temperatures ( $1 - \sigma$ ) from HRC-I countrates, assuming the carbon atmosphere model spectrum. Lineaer fitting indicates a decline of  $2.0^{+1.0\%}_{-1.0\%}$  over 10 years (with  $1 - \sigma$  errors). The linear fit is poor with  $\chi^2$  of 40 for 17 degrees of freedom. 45
- Figure 4.11 The measured temperatures ( $1 - \sigma$ ) from ACIS-S (FAINT) for the neutron star in Cas A, assuming the carbon atmosphere model spectrum. Linear fitting indicates a decline of  $1.5^{+2.0\%}_{-2.0\%}$  over 10 years (with  $1 - \sigma$  errors). The linear fit is with  $\chi^2$  of 9.3 for 16 degrees of freedom. 46

Figure 4.12

The inferred drop in surface temperature of the neutron star in Cas A from all detectors on *Chandra* over 10 years. The ACIS-S GRADED result from [Heinke and Ho](#) has been shifted to 2.8% instead of 3.6%, as suggested by recent *Chandra* calibration efforts. The result from HRC-S puts a lower limit of 1.5% on the cooling. The results from HRC-I, ACIS-I and ACIS-S FAINT observations have various systematic problems, as discussed in the text. [47](#)

---

## ACRONYMS

---

ACIS	Advanced CCD Imaging Spectrometer
APR	Akmal-Pandharipande-Ravenhall
ARF	Auxiliary Response File
CTI	Charge Transfer Inefficiency
EOS	Equation of State
HRC	Resolution Camera
HRMA	High Resolution Mirror Assembly
ObsID	Observation ID
PBF	Pair Breaking and Formation
PSF	Point Spread Function
RMF	Redistribution Matrix File
QE	Quantum Efficiency

---

## INTRODUCTION - THE WHAT?

---

### 1.1 LIFE STORY

The key element in the universe is hydrogen as it is the main element involved directly or indirectly in forming stars, keeping them alive or finishing their lives. Stars start their lives in dark, cold and dense gas clouds ( $\sim 10$ - $100$  pc across) with temperature  $10$ - $20$  K [55]. At these cold temperatures the gas is in a molecular form such clouds, called molecular clouds composed *mainly* of  $H_2$ , CO molecules and dust grains [68].

The density within the cloud is not homogeneous, due to several reasons such as; expanding shock waves from nearby explosions, the spiral motion of the galaxy that compresses material, ... etc. These effects can compress the gas in the cloud and consequently increase the density in some regions [6]. The cloud can remain at equilibrium only if supported against the inward collapse (from the gravitational potential energy  $E_G = -3GM^2/R$ ) to higher density by the internal pressure from the thermal kinetic energy of the particles within the cloud ( $E_k = 3NkT/2$ ). However, if the mass of a region in the cloud reaches a critical mass limit called the *Jeans Mass*  $M_J \propto \rho^{-1/2}T^{3/2}$ , it can not be further supported by  $E_k$  and will gravitationally collapse on itself [6].

This Jeans instability gives rise to fragmentation patterns in the cloud, starting its collapse. The mass of the collapsing fragment is a factor in the time-scale of the birth process, where the more massive fragments collapse more rapidly, a solar mass star collapses in around few  $10^5$  years in this stag [35].

Once the protostar's central temperature and pressure are high enough, nuclear fusion starts and it becomes a real star. Nuclear fusion starts by fusing Hydrogen to Helium nuclei, releasing huge amounts of energy that slow the collapse and eventually bring the star into hydrostatic equilibrium — it generates sufficient pressure to balance the pull of gravity [59].

When the temperature reaches  $\sim 10^7$  K in the core, hydrogen ignition starts via the proton-proton chain. First a proton fuses with another proton to form a deuteron (nucleus of deuterium, a proton plus a neu-

tron), which in turn fuses with another proton to form  ${}^3_2\text{He}$ . Finally two  ${}^3_2\text{He}$  atoms will fuse to form  ${}^4_2\text{He}$  and two protons, plus a release of energy [59]. The energy released during fusion, is that it provides the star with an outward radiation pressure support it against gravitationally collapse. The star continues to fuse Hydrogen to Helium for amount of time that depends principally on the mass of the star. Massive star live for shorter times, as they burn Hydrogen in the core faster, which is *only* of order a few tens of million years for stars above ten solar masses ( $10 M_{\odot}$ ) [41]. After the star consumes all the Hydrogen in the core and converts it into Helium, it triggers Hydrogen burning in the outer shells of the core. This shell burning will cause the star to expand (for reasons that are still not fully understood). The expansion of the star dramatically increases the star's surface area. Although its luminosity also increases dramatically, the increase in surface area is larger, leading to a decrease in temperature, and the star becomes what is known as a red giant.

For stars of the Sun's mass or greater, the central temperature and pressure reach high enough to ignite the burning of helium into carbon in the core, followed by a second shell-burning phase and second ascent of the giant branch [54]. If the mass of the star is below  $\sim 8 M_{\odot}$ , the burning shells eventually cool and leave behind a stellar remnant, a hot and degenerate core called a white dwarf, which gradually cools down and is supported against collapse by the pressure of degenerate electrons [48]. There is a limit to the pressure that degenerate electrons can sustain, due to the relativistic limit on the velocity that electrons can attain, which leads to a maximum mass (the Chandrasekhar mass) for white dwarfs, of  $\approx 1.4 M_{\odot}$  [57].

## 1.2 SUPERNOVA

The fate of any star depends crucially on its mass. Massive stars  $\gtrsim 10 M_{\odot}$  reach higher core temperatures that trigger further nuclear burnings beyond Carbon to heavier elements reaching the iron peak. This results in a core mainly composed of  ${}^{56}\text{Fe}$  surrounded by other heavy elements e. g. silicon, oxygen, neon, carbon [48]. As the mass of the core increases, approaching close to the  $M_{\text{Ch}}$  limit, the degenerate electrons can no longer support the collapse, and the core collapses on a free-fall time scale of only  $\sim 7 \times 10^{-3}$  s [57].

The core will then continue to collapse until the density is comparable to the density of atomic nuclei  $\rho_0$ , when the collapse may halt due to the degeneracy pressure between nucleons. This results in a shock generated in the star that catastrophically expels most of the stellar matter, known as a *supernova* explosion. The dense core remains behind, as a compact remnant, either a neutron star or a black hole. The supernova produces a huge energy release of order  $\times 10^{46}$  J, and reaches high lumi-

nosities  $\sim 10^{10}L_{\odot}$ . Take months to fade from visibility. The front shock of the explosion sweeps up the interstellar medium and heats it up to over  $10^7$  K, triggering X-ray emission. The spectrum of the supernova can reveal the elements within the progenitor star. Detailed modeling of supernovae can not yet explain all the observed features and varieties of supernovae. However, we can classify most supernovae into one of several cases:

**Type I:** where Hydrogen is absent in the *visible* spectrum. This type has three sub-cases: Ia: which is associated with close binary systems consisting of a primary white dwarf and a secondary star. The white dwarf accretes matter from the secondary (either by pulling matter from the surface of a non-degenerate star, or by merging with a lower-mass secondary white dwarf), leading to thermonuclear ignition of the white dwarf's fuel. However, this scenario is controversial [7]. The lack Hydrogen lines in the spectrum is because the white dwarf is composed of heavy elements. The other subtypes are Ib and Ic which are associated with the collapse of a massive star (as Type II below) that has blown away its hydrogen envelope, leaving only the massive core.

**Type II:** When Hydrogen is present in the spectrum and dominant. These result from the core collapse of a massive progenitor that is rich in Hydrogen. These are observed usually in regions that have recently formed massive stars. This type of supernovae often produces a central remnant of a neutron star or black hole.

### 1.3 FORMATION OF NEUTRON STARS

When the progenitor star is massive enough ( $\sim 8\text{-}30 M_{\odot}$ ), the birth of a neutron star becomes very likely [48]. The formation of a neutron star goes through interesting stages, which can be summarized as follows:

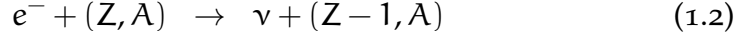
Because the core is massive and at high densities, the very high central temperature  $T_c \propto \rho^{1/3}M^{2/3}$  will ignite silicon burning which result in enriching the core with the iron group ( $^{56}\text{Fe}$ ,  $^{58}\text{Fe}$ , ...). The mostly iron core of the star, has a typical mass of  $M_{\text{core}} \approx 1.4M_{\odot}$ , supported by the pressure of the degenerate electrons [57].

During the later burning stages, the temperature becomes high enough to lead to breakup of nuclei (so-called photodissociation) and their re-formation, e.g.;



As the core becomes mostly iron, further burning does not produce additional energy, so the core cannot support itself and begins to col-

lapse. As the density increases up to full electron degeneracy, it becomes energetically favored for nuclei to capture electrons;



This removes electron degeneracy pressure support from the core, speeding the collapse [57].

As the neutronization process continues, neutrons can undergo the standard  $\beta$ -decay process to produce protons, electrons and anti-neutrinos. However at this stage where density exceeds  $4 \times 10^{17} \text{ g cm}^{-3}$  [57], the electron degeneracy becomes complete leaving no extra vacant quantum energy states for electrons to occupy, therefore because of Pauli exclusion principle, neutrons cannot decay any more back to electrons and protons. To bring the system to equilibrium, neutrons can leak out of the nuclei in what is called *neutron drip* to bring the minimum energy arrangement of the mixture of the neutron-rich nuclei, non-relativistic degenerate neutrons and relativistic degenerate electrons to equilibrium. In other words, as long as the Fermi energy of neutrons is less than the Fermi energy of protons and electrons, they cannot decay. This gives rise to a high ratio of neutrons to protons of  $\sim 200 : 1$ , allowing the star to be supported against gravitational collapse by the degeneracy pressure of the relativistic neutrons [66].

Eq. (2), (3) and several other thermal emission processes (e. g.: annihilation processes) result in releasing huge amount of neutrinos [57]



where they get trapped temporarily, mainly via free nucleon scattering and nucleon absorption. The typical cross section for the neutrino trapping reactions are of order  $\sigma_\nu \sim 10^{-40} \text{ cm}^2$  which gives a mean free path for the neutrinos of order  $\lambda_\nu \sim 10 \text{ cm}$  [66], which is much smaller than the radius of the neutron star, which is several kilometres. As the density of the core increases, the gravitational collapse will stop when the density reaches the nuclear density  $\rho \simeq \rho_{\text{nuclear}} \simeq 2 \times 10^{20} \text{ g cm}^{-3}$  [48].

The newly born neutron star reaches a temperature of  $\sim 10^{11} \text{ K}$  for a few tens of seconds, until the neutron star becomes optically thin for the neutrino stream which carries energy away allowing the temperature drops to  $\sim 10^7 \text{ K}$  [66]. The emission of neutrinos is the main method by which the neutron star is able to cool down.

The name *neutron star* is a little bit misleading, since a *pure* neutron matter does not exist [40]. The neutron star is born with plenty of pro-

tons in the core, but neutrons dominate eventually. However, the composition throughout the star is not homogenous, it likely constructs of different layers [48]. The exact internal structure of neutron stars is not very certain [48]. The relation of the pressure inside the neutron star as a function of density  $P = P(\rho)$  giving the the equation of state (EOS) of the neutron star.

The structure of the neutron star can be mainly decomposed to three regions that differ in density, thickness and composition: *Atmosphere*, *Crust* and *Core*.

Atmosphere:

The neutron star atmosphere is a thin blanket layer a few centimetres thick [46]. The thickness of the atmosphere layer depends on the temperature and surface gravity of the neutron star's surface. It is composed of the lightest elements present, which float to the top, such as H and He [69]. However, a recent discovery [25] revealed that the neutron star in Cassiopeia A has a thin non-magnetized carbon atmosphere. This is discussed in details in [Section 3.3](#).

Crust:

The crust is divided into an outer crust and an inner crust. The outer crust extends for a few hundreds of meters below the atmosphere and is composed of ions and degenerate electrons [32]. The density in this region increases with depth, reaching a density of  $4 \times 10^{11} \text{ g cm}^{-3}$ , sufficient for inverse  $\beta$ -decay and thus the presence of free neutrons, at the boundary with the inner crust [57]. The inner crust extends for about one kilometre reaching a density  $\sim 0.5\rho_0$  at its bottom, where  $\rho_0$  is the density of atomic nuclei,  $2.8 \times 10^{14} \text{ g cm}^{-3}$  [32]. The matter in the inner crust consists of electrons, increasingly neutron-rich nuclei, and increasing numbers of free neutrons. At the bottom of this region, the nuclei dissolve into a sea of free protons and neutrons [48].

Core:

This is the largest part of the neutron star, extending of order 10 km in radius, with densities ranging from  $\sim 0.5\rho_0$  to  $2\rho_0$  [57]. It is mainly composed of neutrons, protons, electrons and muons, all in degenerate states. The EOS for this state of matter remains uncertain as the many-body problem for strong nuclear forces is not well-developed yet [48]. The electrons and muons in this region form almost an ideal Fermi gas, while neutrons and protons form a strongly interacting Fermi *liquid* that may be a superfluid [32]. An inner core would be defined as occurring at very high densities,  $\sim 10\rho_0$ , where alternative arrangements of quarks may possibly condense into exotic particles, e.g. hyperons or kaons [57]. Not all neutron stars would necessarily have inner cores, as lower-mass neutron stars may not reach these high densities, and thus may not pro-

duce exotic particles in their cores [32].

Neutron stars exhibit many interesting features, one of which is that they can display radio pulsations; such neutron stars are known as *pulsars*. In 1967, J. Bell and A. Hewish discovered a radio source that pulsed every 1.33 seconds, rapidly followed by other similar pulsating sources of radio, which they named pulsars.

Baade and Zwicky had previously (1934) predicted the formation of neutron stars as remnants in supernovae, a term they coined and suggested as a mechanism to convert the potential energy released in producing a neutron star into a stellar explosion. T. Gold and F. Pacini each proposed (1968) that the pulsars were rotating neutron stars. The identification of the Crab Pulsar in the Crab Nebula supernova remnant by R. Lovelace et al. in 1968, with a rotational period of only 33 ms, secured the identification of pulsars as rotating neutron stars, as well as their connection with supernovae. Only neutron stars can rotate with such high frequencies because material at the equator of a white dwarf spinning at such frequencies would not be held down by gravity. The maximum angular velocity a star can rotate at is constrained by the mass and the radius of the star,  $\Omega^2 r = GM/r^2$ . This puts a minimum limit on the period,  $P_{\min} = (3\pi/G\rho)^{1/2}$ , where  $\rho$  is the mass density. White dwarfs do not have the required  $\rho$  to acquire millisecond periods.

#### 1.4 THE COOLING OF NEUTRON STARS

Neutron stars encounter three main cooling stages. The first stage is shortly after the formation of the neutron star when it is between 10 and a few hundred years old, when it has not yet become thermally relaxed. In this stage the core cools via neutrino emission to become cooler than the crust. The outer parts of the neutron star cool as a cooling front propagates outward through the star.

The second cooling stage occurs at ages of  $\sim 10^5$  to  $10^6$  years [33], when the neutron star has become thermally relaxed to an effective temperature  $T_{\text{eff}}$ . This stage is dominated by cooling and from neutrino emission from the core. The final stage is when the old, relatively cold neutron star cools principally via the emission of thermal photons from its surface. Most of the isolated neutron stars that we can observe are in the second stage of cooling, including the neutron star in Cassiopeia A [67].

The core cools due to neutrino emission processes called Urca process where particles are thermally excited to undergo  $\beta$ -decay and inverse  $\beta$ -decay as follows [66]:

$$n \rightarrow p + e^- + \bar{\nu}_e \quad (1.6)$$

$$p \rightarrow n + e^+ + \nu_e. \quad (1.7)$$

The direct Urca process is a very fast cooling mechanism, however this process takes place only when the ratio of protons to neutrons,  $\chi$ , exceeds 1:8 [66]. Although this ratio increases when increasing the density, but  $\chi = 1 : 8 \approx 11\%$  is still higher than the value predicted by neutron star equations of state even at high densities near the nuclear density where  $\chi \approx 5\%$  [40]. The direct Urca process needs very high density to be triggered, hence it is forbidden for low mass neutron stars as the density does not reach to the threshold density to start the direct Urca. The threshold density for the direct Urca process depends crucially on the equation of state of the neutron star. For the APR equation of state, the critical mass that would allow direct Urca process is  $1.97M_\odot$  [40], other EOS's have different critical masses.

However, another *modified* Urca process takes place when the direct Urca process is not possible [66]:

$$n + N \rightarrow p + N + e^- + \bar{\nu}_e \quad (1.8)$$

$$p + N \rightarrow n + N + e^+ + \nu_e \quad (1.9)$$

Where N is another proton or neutron that takes part in the reaction to sustain the conservation of momentum.

The modified Urca process is 6-7 orders of magnitude slower than direct Urca [40]. The internal temperature of the neutron star and the neutrino cooling rate depend on the composition of the core. There are other theoretically predicted neutrino cooling processes that require other particle components in the core [67]. Some EOSs predict Bose-Einstein condensates of pions or kaons may appear at high densities, while others permit rearrangement of quarks into hyperons at high densities [40]. These condensation would allow other URCA-like neutrino emission processes that involve rearrangements of quarks, to make these exotic particles.

The behaviour of the cooling also depends on the composition and thickness of the outer crust, which affect the heat conduction [66]. The critical functions for determining the cooling (neutrino luminosity, effective temperature, etc.), can only be tested by comparing theoretical cooling curves with observations.

In the standard cooling scenario the surface temperature ranges from  $3 \times 10^5$  to  $10^6$  K [40]. This suggests that much of the emission will be in the X-ray regime, which can be observed with current X-ray telescopes such as the Chandra X-ray Observatory. The thermal emission takes place at an effective temperature  $T_{\text{eff},\infty}$ . However, neutron stars are *not*

perfect blackbodies, as discussed in [Section 1.3](#). They have a thin atmosphere which is difficult to model [69]. Observing thermal emission from neutron stars, and modeling that emission, has been a significant scientific enterprise for several decades.

---

*Chandra* X-RAY OBSERVATORY - THE HOW?

---

## 2.1 X-RAY ASTRONOMY

There are many sources and phenomena in the universe that produce X-rays. X-rays can be produced when matter reaches very high energies, which can be found in different systems such as relativistic electrons moving in high magnetic fields, accretion disks in very high gravitational fields, or explosions. Thus, probing the universe in X-rays is important to understand how such systems work. Since X-rays are absorbed in the Earth's atmosphere, observing cosmic X-ray photons must be done from space.

X-rays from the solar corona were discovered by a detector on a 336-second rocket flight in 1949 [16]. X-rays from outside the solar system were first observed by detectors on rockets in 1962 when the X-ray source Sco X-1 was discovered, along with a diffuse X-ray background from numerous fainter sources [17]. Further study showed that Sco X-1 was most likely an accreting neutron star [56].

The first X-ray mission to orbit the Earth was the NASA satellite *Uhuru* in 1970, observing in the energy range 2-20 keV [18]. *Uhuru* discovered diffuse X-ray emission in galaxy clusters [34], X-rays from radio pulsars, supernova remnants and active galactic nuclei [15], and confirmed the accreting neutron star in stellar binaries nature of some X-ray sources [56]. In 1978, NASA launched the first X-ray imaging satellite *Einstein* (that is, the first to focus X-rays into an image, rather than using a collimator or coded mask to identify source positions). X-ray imaging requires that the paths of X-rays are only deflected by a few degrees (lest they be absorbed). *Einstein* had an excellent set of X-ray mirrors, a high-resolution imager reaching angular resolution of 2 arcseconds (denoted  $''$ ), and the first high resolution spectroscopy, which used a crystal to spread out X-rays by wavelength <sup>1</sup>. Numerous other X-ray missions have pioneered new technologies, including the Japanese *ASCA* satellite in 1993, the first to use a charge-coupled device (CCD) to measure the energy of each X-ray in an image with high precision <sup>2</sup>.

---

<sup>1</sup> <http://heasarc.gsfc.nasa.gov/docs/einstein/hea02.html>

<sup>2</sup> <http://heasarc.gsfc.nasa.gov/docs/asca/asca.html>

## 2.2 CHANDRA X-RAY OBSERVATORY

Here we summarize the relevant information about the Chandra X-ray Observatory necessary to understand this thesis. Except where another source is cited, the reader may take the Proposer's Manual <sup>3</sup> as the source for material in this chapter.

The Chandra X-ray Observatory was launched in 1999 to observe X-ray sources with higher angular resolution (half of the power from a point source falls within a radius of 0.5", four times better than *Einstein's* previous record), spectral resolution, and sensitivity (for an imaging X-ray telescope) than previous instruments. Chandra includes high-precision mirrors and two detectors (each arranged in two arrays), the Advanced CCD Imaging Spectrometer (ACIS) arrays of CCDs, and the High Resolution Camera (HRC) arrays of microchannel plates. In addition, Chandra has an optical telescope (used to identify stars and precisely track Chandra's position), and two arrays of gratings that can be slid into the path of the X-rays. to spread the light of bright targets by wavelength. Although there are observations of our target Cas A using these gratings, these observations are exceptionally difficult to analyze, for our science goals we do not analyze them or discuss the gratings further here.

## 2.3 HIGH RESOLUTION MIRROR ASSEMBLY (HRMA)

The process of focusing X-ray photons is different from optical telescopes. In optical telescopes the photons are focused when reflected by a primary curved mirror. But X-ray photons will simply penetrate the same mirrors. In the case of X-ray photons, the mirrors must be *almost* perpendicular to incident X-ray photons, allowing photons to graze the surface of the mirror like a stone grazing the surface of a lake. The focusing of X-ray photons depends on the energy of the x-ray photon and the grazing angle. The higher energy the photon, the longer the required focal length.

The HRMA consists of 4 pairs of thin-walled nested concentric mirrors coated with iridium with a binding layer of chromium. The front mirror of each pair is a paraboloid and the back is hyperboloid. The geometry (known as Wolter Type 1) allows a small ring of photons to enter the front of the telescope, be slightly reflected from the front mirror of each pair, and be reflected again by the back mirror, being brought to a focus at the detector plane. Each pair of mirrors thus increases the effective area of the telescope.

The HRMA are the smoothest X-ray mirrors ever designed, reducing random scatters of X-rays to produce the sharpest X-ray images. However, the angular resolution of these images increases with angle from

---

<sup>3</sup> <http://cxc.harvard.edu/proposer/POG/>

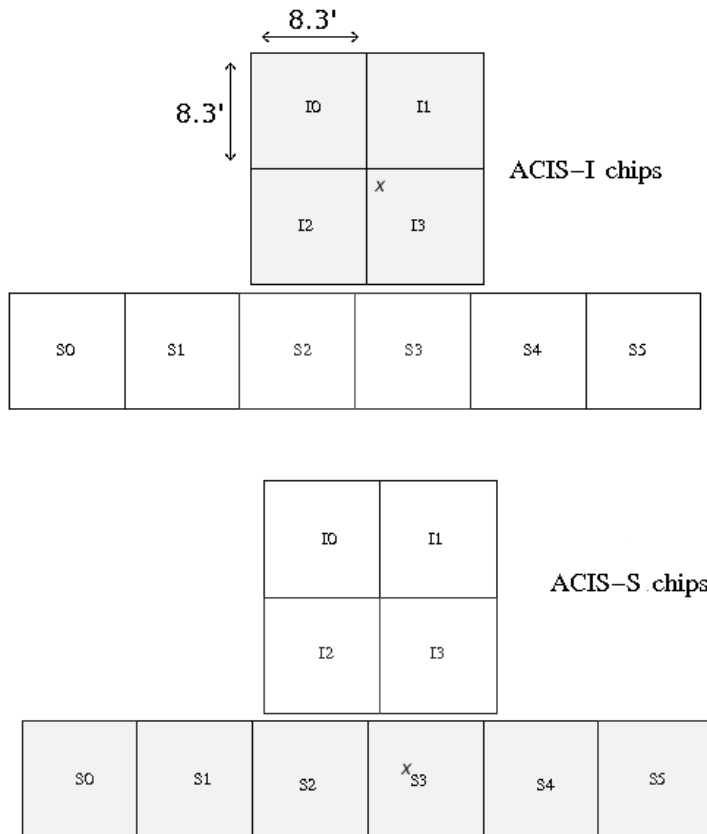


Figure 2.1: The Advanced CCD Imaging Spectrometer (ACIS) detector on *Chandra*. It has two detectors; ACIS-I optimized for imaging and ACIS-S optimized for spectroscopy. ACIS can be used with the High Energy Transmission grating to give high spectral resolution. The aim-points are marked with (×). Figure from (<http://cxc.harvard.edu/cal/Acis/>)

the optical axis blurring the image. On-axis, 90% of the light from a typical source falls within a circle of radius 1". At an angle of 4 arcminutes (4') off-axis, the equivalent circle is 2" in radius, and at 8' off-axis it is ~8" in radius.

### 2.3.1 Advanced CCD Imaging Spectrometer (ACIS)

The ACIS detector consists of 10 planar CCDs. Each CCD has  $1024 \times 1024$  pixels, and covers  $\sim 8 \times 8$  arcminute field of view (each pixel is 0.492" per side). Four of these are arranged as a  $2 \times 2$  array, called ACIS-I, that is optimized for imaging purposes. ACIS-I covers a  $16 \times 16$  arc minutes field of view, with chips tilted to match the *Chandra* focal surface. The other six CCDs, called ACIS-S, are arranged in a  $1 \times 6$  array that is optimized for readout from the transmission grating to obtain high resolution spectra. The ACIS detector features the best energy resolution on *Chandra*, as low as 95 eV at 1.49 keV, without the case of

grating, the ACIS detector energy range extends between 0.08 to 10.0 keV, with the highest effective area between 0.7 and 5 keV. The CCDs on ACIS feature a blocking filter made of aluminum and plastic which blocks most optical photons, as the CCDs are also sensitive to light.

The ACIS-I detector consists of four chips labeled I<sub>0</sub>, I<sub>1</sub>, I<sub>2</sub> and I<sub>3</sub> and ACIS-S chips are labeled as S<sub>0</sub> to S<sub>5</sub> (see [Figure 2.1](#)). Two chips, S<sub>1</sub> and S<sub>3</sub>, are back-illuminated chips and the rest are front-illuminated chips. CCDs in general are composed of silicon and the pixel boundaries are defined by a gate structure on the surface of the CCD. The front-illuminated chips have a gate structure facing the incident X-ray photons, while the back-illuminated chips have a gate structure on the back side of the chip. In practice, the back-illuminated CCDs show higher efficiency in detecting photons at low and medium energies, but suffer higher background rates. The higher efficiency of the back-illuminated CCD has meant that the ACIS-S detector, with its aimpoint on a back-illuminated detector, has been the detector of choice to study objects less than 8' in size.

After a photon hits the silicon on the CCD, this causes photoelectric absorption in the silicon that frees electrons. The number of liberated photons from the silicon atoms is roughly proportional to the incident photon energy. As soon as this electron charge is formed, it then gets confined by electric fields in a small volume near the interaction site. X-rays (or non-X-ray background, such as cosmic rays) may free electrons on multiple adjacent pixels, which are grouped together by software and identified as a single event.

The CCD is exposed for a frame-time of typically 3.2 seconds, then read out by a series of voltage changes which shuffle the charges from one pixel to the next, each shuffle taking 0.040 ms (so for 1024 rows, a total of 41 ms). During this shuffle, if there are defects in the semiconductor, some electrons may get stuck in a defect, and released later or not at all. This causes degrading of the energy resolution and other difficulties (see below). This loss of electrons is called charge-transfer inefficiency (CTI). The data arrive in the frame store region (not exposed to sky), and are then transferred to a local processor which identifies the position and the amplitude of these events. An event requires a local maximum for the energy of the charge distribution that is larger than the threshold energy ( $\sim 150\text{eV}$ ) when subtracting the bias, which is the amplitude of the charge in each pixel in the absence of external radiation.

When the X-ray photons are detected on the CCD, an on-board process examines all the pixels on the CCD and then selects the events that matches the criteria of those above the threshold energy and local maximum, then reads the surrounding  $3 \times 3$  pixels and assigns a "grade" to

the pattern of charge, depending on the geometry of which pixels are above the threshold energy. Grades distinguish *good* from *bad* data, by separating geometries typical of X-ray photons from geometries typical of cosmic rays, which have higher energies and enter the detector from all directions. Some particularly “bad” grades are not included in the telemetry stream, but the majority are included.

Data telemetry can be put into different formats, for different trade-offs between background rejection efficiency and total telemetry rate. In *faint* format the amplitude of the signal in each pixel of the  $3 \times 3$  surrounding island is telemetered, along with the event grade. In *graded* format, only the total energy and grade of each event, not the amplitude of signal in each pixel, is telemetered. Finally in the *very faint* format the events are still graded by  $3 \times 3$  pixels, but this format provides data for pixel values in a  $5 \times 5$  pixel island around the local maximum. The very faint format allows for more careful background cleaning, at the price of higher telemetry rates per photon, and thus is limited to fainter objects. Detailed processing of faint (or very faint) format data can identify some “bad” grade events that are real X-ray photons. For instance, CTI tends to delay the arrival of some electrons, shifting the pattern of charge and thus turning “good” events into “bad” ones. An algorithm has been developed to counter the effects of CTI, using information from the  $3 \times 3$  pixel island, so obviously cannot be used on the on-board graded format data.

The quantum efficiency of front-illuminated chips is lower at low to medium energies. The combined HRMA/ACIS on-axis effective areas (thus, including the mirror reflectivity and the CCD quantum efficiency (plus the effects of the optical blocking filter) are shown in [Figure 2.2](#).

For high count rates the CCDs on ACIS will be likely be piled up. Pileup is an effect where two or more photons land on the CCD in the same or adjacent pixels during one frame time, and are thus detected as a single photon. This can lead to distortion of the energy spectrum, as the detected photon energy will be essentially the sum of the piled up photons. This also would cause a lower inferred count rate. The pileup can also lead to other problems such as grade migration or pulse saturation. The grade migration is the change of grade from *good* to *bad* as an effect of pileup. Pulse saturation is a consequence of high pileup, where the total amplitude of the photons in the event is larger than 13 keV which is automatically rejected and not telemetered. A pileup-correction algorithm (for low levels of pileup) was developed by [Davis](#), and has been implemented in different spectral analysis software such as XSPEC, Sherpa and ISIS. By choosing to read out only a subset of the detector rows (a subarray), the user may reduce the frametime, thus reducing the amount of pileup (and permitting a higher rate of telemetry per event), at the cost of a reduced field of view.

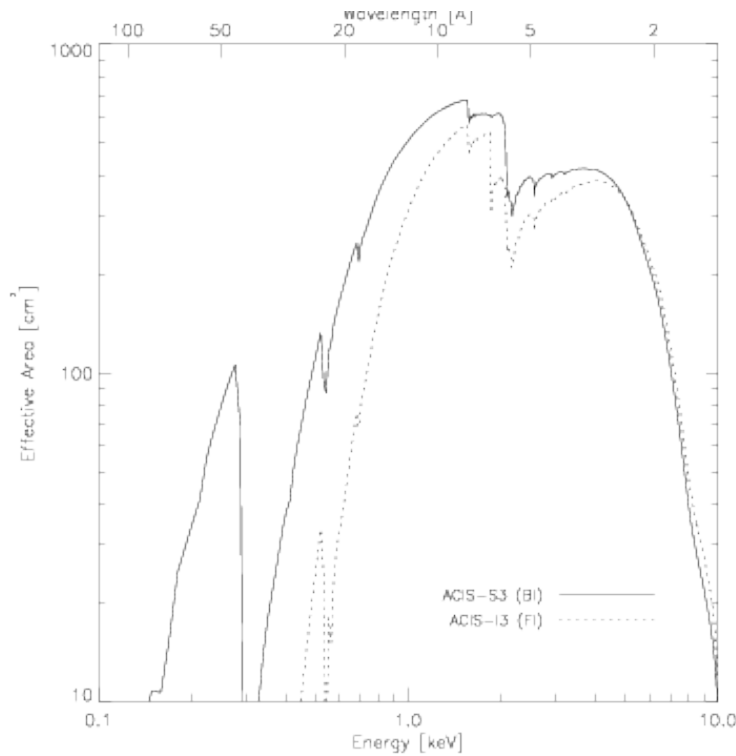


Figure 2.2: The combined effective area of HRMA/ACIS at different energies. Figure from (<http://cxc.harvard.edu/proposer/POG/html/chap6.html>).

### 2.3.2 High Resolution Camera (HRC)

The High Resolution Camera (HRC) is a microchannel plate (MCP) detector. The HRC detector energy range is slightly below the energy range of ACIS (0.06-10 keV) but with poor energy resolution as  $\delta E/E \sim 1$  at 1 keV. The HRC detector offers the best time resolution  $16\mu\text{s}$ . HRC contain two detector arrays. HRC-I is optimized for imaging with the largest field of view on *Chandra*,  $30 \times 30$  arc minutes. HRC-S is optimized to read out a spectrum spread out by the low energy transmission grating, and has a  $9 \times 99$  arc minutes field of view (See Figure 2.3). Both detectors have very good spatial resolution ( $\sim 0.4''$ ), slightly better than ACIS due to their  $0.1''$  pixel size, so the angular resolution is set by the mirrors.

The method for detecting X-ray photons on a microchannel plate is different from the CCD. The HRC is shielded against UV light and ions to permit only X-ray photons to pass to the MCP which is coated with Cesium Iodide (CsI). The side walls of the HRC also block high energy X-rays, and by measuring time coincidences of detections in the side walls vs. the detector, can reject the majority of cosmic rays. The incident photon passes through a first input MCP in which there are millions of small tubes tilted at angles of  $6^{\text{deg}}$  from the oncoming photon direction.

## Focal Plane Layout

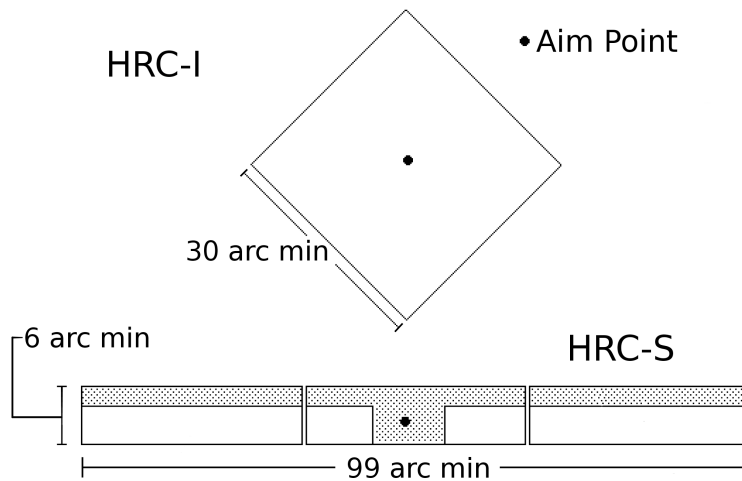


Figure 2.3: The High Resolution Camera (HRC) microchannel plates (MCP) offer the highest spatial resolution (0.4"). The HRC consists of two detectors, HRC-I, which is optimized for imaging and HRC-S, which is optimized for high-resolution spectroscopy when used with the Low Energy Transmission Grating (LETG). Figure from (<http://cxc.harvard.edu/cal/Hrc/index.html>)

The photons are absorbed by the CsI on the walls of the tubes, releasing photoelectrons which are accelerated by an applied electric field. The photoelectrons then go through a second output MCP which contains millions of smaller tubes, biased at the same angle in the opposite direction to increase the probability of photoemission process. This results in releasing a cascade of electrons which are accelerated toward a crossed grid charge detector. The position of the incident X-ray photon is the centroid of the electron cloud leaving the output MCP. The amplitude of the cascade of electrons has only a limited correlation with the input photon energy, leading to the poor spectral resolution of the HRC.

The quantum efficiency of HRC-S is of complex structure and has decreased  $\sim 10\%$  over the duration of the *Chandra* mission at ( $\lesssim 1\%$  / year). This quantum efficiency decline is apparently wavelength independent. The HRC-I quantum efficiency is known to have been decreased  $< 2\%$  over the duration of the *Chandra* mission <sup>4</sup>. The HRC-S has substantially higher background than HRC-I, due to the failure of the anti-coincidence detector (detections of cosmic rays in the walls are not correctly associated with events in the detector).

Since there is no frame time, the intrinsic timing resolution of HRC is quite good (16 microseconds). However, due to a wiring error, the time of an event is incorrectly associated with the following event. If the following event may not telemetered to ground, then the timing resolution

<sup>4</sup> <http://cxc.harvard.edu/ccw/proceedings/2007/presentations/possonbrown3/>

becomes essentially the mean time between events, or no less than  $\sim 4$  milliseconds. To achieve high time resolution (for use with rapidly spinning neutron stars), Chandra operations developed a “timing” mode for HRC-S, in which only a portion ( $1/3$ ) of the HRC-S detector is read out, thus preventing telemetry saturation.

---

## CASSIOPEIA A - *THE WHY?*

---

### 3.1 THE SUPERNOVA REMNANT

The Cassiopeia A supernova remnant is the second youngest known supernova remnant in our galaxy, and the youngest to contain a known compact object <sup>1</sup>. It may have been observed in 1680 AD by the British astronomer Flamsteed, at only 6th magnitude <sup>2</sup>. The time scale of the expansion of the optical supernova remnant measured by van den Bergh and Kamper [64] is consistent with the  $\sim 330$  year historical age. The supernova remnant is one of the brightest sources in the sky in radio and X-ray, but is relatively faint in the optical band.

The Cas A supernova remnant is almost spherical with radius  $\sim 2.5'$ . It has strong synchrotron emission in the radio band from high-energy electrons [5], emission lines in the optical from dense knots of cooling plasma [61], and infrared emission from shock-heated dust [52]. In the X-ray, three components are detected; thermal X-rays from the exploded stellar interior [26], nonthermal hard (=high-energy) X-ray emission from high-energy particles [20], and a compact stellar remnant at the center [60].

More than 100 fast moving knots show strong emission lines of oxygen, sulphur and argon, and move with high radial velocities  $\sim 5 \times 10^3$  km s<sup>-1</sup> and large proper motions  $\mu = 0.2'' - 0.7''/\text{year}$  [63]. Comparing the proper motion (angular velocity) of knots at the remnant edge, vs. radial velocities of knots at the projected center (coming towards or away from us), allows us to infer the true velocities corresponding to an angular velocity, and thus to infer a distance of  $3.4_{-0.1}^{+0.3}$  kpc [50].

In the northeastern side of the supernova remnant, a clear jet-like feature of sulfur-rich ejecta extends beyond the other ejecta, to around  $\sim 4'$ . Another feature of  $\sim 36$  quasi-stationary flocculi are present with lower radial velocities and proper motion than the fast moving knots, containing strong emission lines of nitrogen and helium. These quasi-stationary flocculi are thought to constitute stellar material lost by the progenitor star [12]. The supernova remnant is rich in oxygen, which indicates that

---

<sup>1</sup> The youngest known supernova remnant is G1.9+0.3 near the galactic center with an age of  $\sim 100$  years [51]

<sup>2</sup> Due to obscuring dust in this line of sight, it was nowhere near as bright as other recent supernovae.

the progenitor star was a massive star with a zero-age main sequence mass of  $M \sim 15M_{\odot}$  [31]. Spectroscopy of light echoes (off nearby molecular clouds) from the supernova explosion have enabled identification of the supernova explosion as type IIb; a type II core-collapse in a red supergiant, but with the red supergiant having lost most of its hydrogen envelope before the explosion [31].

Deep X-ray observations of the supernova remnant shows a bright ring of radius  $\sim 110''$  with a thickness of  $\sim 30''$ . This X-ray ring is the progenitor star's ejecta, heated by the reverse shock (the shock penetrating back into the ejecta) to a few million K. This ring shows irregular clumpy emission, reflecting the inhomogeneous nature of the supernova expansion and the interaction with the reverse shock, which also caused radiative cooling instabilities [27]. As the supernova remnant's blast wave moves through the circumstellar material at  $\approx 6 \times 10^3 \text{ km s}^{-1}$  it produces an outer, fainter, filamentary ring with radius  $\sim 150''$ , where particles are being accelerated up to cosmic ray energies [20].

Comparison of X-ray filaments taken between 2000 and 2004 reveals presence of several small-scale features  $< 10''$  that exhibit significant intensity changes. Changes include increases between  $\sim 10\% - 90\%$  in countrate and, in other regions, decreases of  $\sim 30\% - 40\%$  in countrate [43].

### 3.2 CENTRAL COMPACT OBJECT

The central compact object was first seen by Chandra in a spectacular *first light* image in 1999 [60]. The X-ray-to-optical flux ratio is  $> 10^4$ , which strongly indicates that this is indeed a compact object [13], eliminating the possibility of a background active galactic nucleus, for instance. Since the X-ray spectrum of the point source is stable, it also cannot be a black hole, as if this was the case the X-ray emission would be due to accretion, and accretion implies significant variability in the spectrum due to unstable emission processes [47]. Therefore this central compact object is strongly believed to be the neutron star remnant of the supernova explosion.

This point-like source showed no evidence for pulsations (as might be expected from a radio pulsar) in either ACIS or HRC observations [37]. Also, it does not appear in a 20 cm radio map, nor is there an optical counterpart within a radius of  $5''$  around the compact object [45]. Young pulsars surrounded by nebula in supernova remnants usually feature pulsar wind nebula (PWN) where the high energy relativistic particles from the compact object produce X-ray emission. However, in the case of the neutron star in Cas A, there is no extended high energy counterpart, The soft X-ray spectrum of this compact object indicates that the X-ray emission is thermal in nature, and not generated by relativistic particles

in the magnetosphere of the compact object. Therefore, it was concluded that this object is not a rotation-powered pulsar.

Absence of pulsar activity could be caused by a strong magnetic field ( $> 10^{13}$  G) that overcomes the single photon splitting  $\gamma \rightarrow \gamma\gamma$  over the pair production process  $\gamma \rightarrow e^+e^-$  [4]. Such strong magnetic fields are characteristic of “magnetars”, neutron stars often showing strong X-ray pulsations and/or X-ray/gamma-ray flares, and as well as high rates of change of their spin period. Their radiative energy output, in contrast to normal pulsars, is larger than the energy extracted from the rotational spindown of the neutron star, and is thought to be due to decay of the superstrong magnetic field [29]. Although many magnetars are typically rather brighter than the Cas A neutron star ( $L_X \sim 10^{34} - 10^{35}$  ergs/s), several transiently active magnetars (and high-magnetic-field radio pulsars) have been recently identified, with quiescent X-ray luminosities and temperatures consistent with Cas A [29]. No episodes of intense X-ray (or gamma-ray) flaring have been seen from the Cas A neutron star, but our knowledge of magnetars may be biased by selection effects towards the most variable. There is no strong evidence for a magnetar nature for the Cas A neutron star, but definitive evidence against the possibility is also lacking. The strongest evidence against a magnetar nature for Cas A is the information we have about other, similar, young neutron stars in supernova remnants.

The X-ray spectrum of the neutron star (in the initial, shallow Chandra observations) could be fit with absorbed (gas and dust absorption removes low-energy photons, here it removes nearly all photons below 1 keV) blackbody or power-law<sup>3</sup> models, but gave unusual results. Some intrinsic discrepancies between the observed spectrum and the best fit models of either absorbed blackbody or power law are present at higher energies ( $> 4.5$  keV) in high-quality deep spectra [45]. A power-law fit would be appropriate for emission by relativistic particles, but the derived photon index of  $5.2 \pm 0.2$  is quite steep for such emission, and gives a hydrogen column density  $N_H \approx 2.8 \times 10^{22} \text{ cm}^{-2}$  [45] which is higher than the estimated atomic and molecular gas column of ions within 30'' of the compact object [30]. Thus investigators have turned to thermal emission from the neutron star surface for spectral models, represented by blackbody or modified blackbody models.

Because the neutron star has a strong gravitational field, the measured temperature and luminosity will differ between an observer at the neutron star surface and a distant observer, and therefore must be corrected for gravitational redshift ( $z$ ) with a factor  $g_r = 1 + z = (1 - 2GM/Rc^2)^{1/2}$ . The superscript  $\infty$  denotes the measured quantities measured by a distant observer (theoretically at infinity), therefore:  $T^\infty = Tg_r$ ,  $R^\infty = R/g_r$ ,

<sup>3</sup> Power-law models have the number of photons at a given energy  $N(E) = KE^{-\alpha}$ , where  $\alpha$  is the power-law photon index,  $K$  a constant. These models often are used to describe nonthermal emission, from e.g. relativistic particles emitting synchrotron radiation.

and  $L^\infty = Lg_r^2$ . The neutron star is estimated to have a typical mass of 1.4 and radius of 10 km, giving  $g_r = 1.3$ . The estimated bolometric luminosity is  $L_{\text{bol}}^\infty \sim 1.6 \times 10^{33} \text{ erg s}^{-1}$  assuming a hydrogen column density  $N_{\text{H}} \approx 1 \times 10^{22} \text{ cm}^{-1}$ . The blackbody fit yields a temperature of  $T_{\text{bb}}^\infty \approx 7 \times 10^6 \text{ K}$  and an inferred radius (given the known distance of 3.4 kpc) of 0.3 km, rather smaller than reasonable neutron star radii [47], and showed formally unacceptable fits in high-quality data. Adding a second, higher-temperature (and smaller radius) blackbody component (or a power-law component) provides a good fit even to high-quality data, and is motivated by the possibility of a hot spot on the neutron star surface [47] [45].

However, the hot spot scenario has the problem that it predicts the neutron star should show pulsations, as the hot spot rotates. No pulsations have been seen in Chandra ACIS, Chandra HRC, or XMM observations that have been searched for them, with limits on the pulsed flux fraction reaching  $<12\%$  for any period longer than 10 milliseconds [22].

The Cas A neutron star is similar in spectrum, luminosity, and lack of other-wavelength counterparts to nine other central X-ray sources in young supernova remnants, the so-called Central Compact Objects (see Halpern and Gotthelf [22] for a review). Three of these objects show detectable pulsations, with spin periods between 0.1 and 0.4 s and pulsed fractions of 9 to 64%. Timing campaigns on these three neutron stars have measured, or established limits on, their rates of period decrease, which directly constrain their dipolar magnetic field. The inferred magnetic field values are: for Kes 79,  $B = 3.1 \times 10^{10} \text{ G}$  [22]; for 1E1207.4-5209,  $B = 0.99$  or  $2.4 \times 10^{11} \text{ G}$  [23]; and for Puppis A,  $B < 2 \times 10^{11} \text{ G}$  [21]. These fields are well below the fields of magnetars, or even of typical radio pulsars (often  $\sim 10^{12} \text{ G}$ ), leading to the terminology “anti-magnetars” for these objects. This suggests that the Cas A neutron star may also have a low B-field, which will affect the interpretation of its spectrum.

A significantly better fit than a blackbody to the Cas A neutron star X-ray spectrum is a modified blackbody when considering a hydrogen atmosphere on a neutron star with a relatively low magnetic field (for  $B < 10^{10} \text{ G}$ , the B field makes essentially no impact on the observed spectrum). This gives a lower effective temperature vs. the blackbody by a factor of 2 and a significantly larger radius than a blackbody, of  $\approx 5 \text{ km}$  [45]. Increasing the magnetic field gives worse spectral fits, and a smaller radius [47]. As with the blackbody fit, a second, hotter neutron star atmosphere component can be added to the fit, now allowing the cooler component to be emitting from the entire surface, while the hotter component represents a hot spot [45]. However, the lack of pulsations means that the hot spot conundrum remains.

### 3.3 THE MYSTERY OF A CARBON ATMOSPHERE

A good solution to the puzzle has been made by Ho and Heinke [25] when they considered a carbon atmosphere model for the neutron star. The carbon atmosphere model for a  $M \sim 1.6$  solar mass neutron star solved the issue of the emitting radius, as the derived emission radius using this model is  $R \approx 12 - 15$  km which agrees with the theoretically expected radii of neutron stars. This indicates that the emission is from the entire surface of the neutron star, resulting from the cooling surface of the neutron star. The model fits well the deep observational data on Cas A described in Pavlov and Luna and Hwang et al.. Statistically, the carbon atmosphere gives a slightly better fit than other models with  $\chi^2 = 105.3$  for 99 degrees of freedom. The inferred temperature  $kT = 0.155$  keV is slightly less than inferred from the other modified blackbody models with hydrogen ( $kT = 0.241$  keV) or helium ( $kT = 0.241$  keV), and indicates a slightly higher hydrogen column density  $N_H = 1.73 \times 10^{22} \text{ cm}^{-2}$  [25].

The detailed theory for the composition of young neutron star ( $< 10^4$  years) crust and atmosphere is not complete. The surface of the young neutron star is believed to be composed of heavier elements (0 through Fe) from the fallback of the supernova explosion. The neutron star probably accretes lighter elements on the surface from the fallback material of the supernova explosion. Spectral fitting of older neutron stars ( $> 10^5$  years) shows good fit with blackbody model modified with Hydrogen or Helium atmosphere. To explain the presence of carbon (requiring fallback), but the lack of hydrogen or helium (which would rise to the surface in 30 seconds due to gravitational stratification), something must remove the hydrogen and helium. Indeed, Chang et al. showed that at the high temperatures of the neutron star surface shortly after the supernova, hydrogen and helium can fuse to make heavier elements (specifically carbon). In this scenario, later fallback will add hydrogen and helium to a cooler surface, reconstituting a hydrogen atmosphere as is observed for older neutron stars.

The discovery of the Carbon atmosphere and the intent to properly understand the neutron star atmosphere is important to link another key information about young neutron stars, the *cooling*. The photon luminosity we observe by our X-ray telescopes from this neutron star is defined by the thermal connection between the mantle and atmosphere [38] hence, good understanding of the neutron star atmosphere will be useful in understanding the thermal evolution of young neutron stars [67].

### 3.4 DETECTION OF COOLING

A key piece of information in understanding the evolution of young neutron stars and their equation of state is their thermal evolution. This gives direct and indirect clues about many temperature-sensitive properties of the neutron stars such as crust solidification, core composition, etc. As discussed earlier in Chapter 1, neutron stars are born at high temperatures  $\sim 10^{11}$  K and cool mainly via neutrino emission from the core. As a consequence of this rapid neutrino emission, the core becomes thermally decoupled from the crust as it cools faster, this essentially means that the cooling of young neutron stars starts as an inside-to-outside process with the crust being hotter than the core inside. As this *cooling wave* propagates to the crust, the neutron star becomes isothermal on a time scale of  $10 < \tau_{\text{isothermal}} < 100$  years [19], therefore, the neutron star in Cas A (at an age of  $t \approx 330$ ) is assumed to have become isothermal.

Analyzing a number of ACIS-S GRADED archival datasets covering the compact object between 2000 and 2009, and using the non-magnetized carbon atmosphere [25] to fit the neutron star spectra, [Heinke and Ho](#) measured a significant  $3.6 \pm 0.6\%$  decline in the surface temperature of the neutron star from  $2.12 \times 10^6$  K in 2000 to  $2.04 \times 10^6$  K in 2009. This gives a temperature evolution timescale of  $T_s = \delta T_s \sim 280$  years, a 21% decrease in the observed (absorbed) flux, and  $15 \pm 4\%$  decrease in bolometric luminosity. This is a key result in many respects. First, this is the only neutron star where we can measure its temperature changing over time. In other neutron stars where we can only measure the *current* temperature. Another more interesting thing about this result, is that this rapid cooling reflects changes of the one happening in the core.

As discussed in [Negreiros et al.](#) there are three general factors that control the cooling of young hot neutron stars. The first factor is microscopic parameters of the cooling presented in the neutrino emissivity, specific heat and the thermal conductivity of the neutron star. The second factor is macroscopic, presented in the parameters of the neutron star equation of state; mass-radius and density-pressure profiles. The third factor is the boundary conditions which controls how the mantle temperature is connected with the atmosphere. The rapidity of this cooling indicated that it must be connected with microscopic changes in the interior. The possible neutrino emission mechanisms from the core discussed in [Section 3.4](#) could not explain this result. The fastest mechanism, the Direct Urca process  $n \rightarrow p + e + \bar{\nu}$  and  $p + e \rightarrow \nu$ , is very fast, so that the current temperature of the neutron star would be much colder. The decline of 4% in surface temperature over 10 years is significantly steeper than can be explained by the modified Urca mechanism [Yakovlev et al.](#) Essentially, the rapid decline plus current hot state required a recent, dramatic change in the neutrino emission properties of

the neutron star. This question now was clear for theorists: What is the cooling mechanism that can explain this result?

### 3.5 PHYSICAL INTERPRETATION

An approach to the interpretation of the [24] rapid cooling result was made by two theory groups [Page et al.](#) and [Shternin et al.](#). The theory is based on an enhanced neutrino emission mechanism from the superfluid core that results from nucleon pairing [14]. Superfluidity is a state of matter featuring interesting physical properties such as zero friction; the viscosity of the fluid is zero, therefore particles in the fluid can move freely. At *low* temperatures and high densities nucleons can cool enough to form pairs known as Cooper pairs in analogy to the electrons Cooper pairs [9] that form in superconductors that was first proposed by Bardeen, Cooper and Schrieffer (BCS) Theory [3]. The idea of a neutron star having a superfluid core was first proposed by Migdal [36]. Superfluid neutrons cannot form at densities below the neutron drip as the neutrons will be still bounded by the nuclei, but when the neutron drip is reached neutrons become free to move and form a *soap* of degenerate neutrons where they interact via long-range attractive interaction pairing up two neutrons together to form Cooper pairs with singlet configuration  $^1S_0$  resulting in a neutron superfluid in the inner crust. This superfluid is believed to be responsible for observed pulsar glitches (e.g. [1]). At higher densities, the  $^1S_0$  superfluid is disfavored, and a  $^3P_2$ - $^3F_2$  mixed triplet neutron superfluid state resides in the core. No direct evidence had yet been seen for this core superfluid.

The temperature at which the transition occurs to superfluidity is called the transition or critical temperature  $T_C$ . The interesting question here is what the superfluid has to do with the cooling of the neutron star? First, the presence of a superfluid will increase the heat capacity of the neutron star if the temperature of the neutron star is just below the critical temperature but will exponentially quell the heat capacity when the neutron stars cools down to temperatures much lower than the critical temperature. The other interesting effect is that superfluidity will also affect the standard neutrino emission processes that are already cooling the neutron star [66]. As discussed in [Section 3.4](#), the standard neutrino emission cooling mechanisms in the neutron star are either the modified Urca process or the fast direct Urca process and these two cooling processes will be reduced in the presence of superfluidity, Hence one can expect decreasing in the cooling rate as a result of superfluidity [66]. However, the presence of superfluidity causes a new enhanced neutrino emission mechanism to occur  $n + n \rightarrow \nu + \bar{\nu}$ ; each time two neutrons form a Cooper pair they release a neutrino and antineutrino.

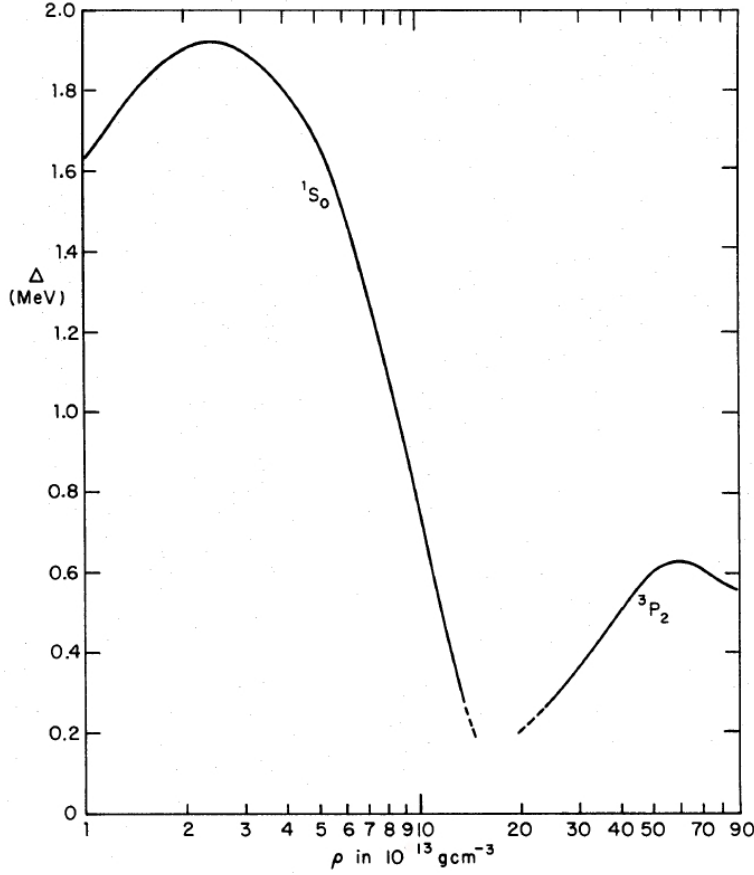


Figure 3.1: Superfluid energy gap  $\Delta$  versus different densities for the  $^1S_0$  and  $^3P_2$  configurations. At lower densities (e. g. the inner crust) the superfluid are paired up at  $^1S_0$  with higher energy gap. As the density increases in the core ( $> 10^{14} \text{ g cm}^{-3}$ ) superfluid neutrons are paired up in  $^3P_2$  configuration. Figure from [53].

There are three possible configurations for neutrons in superfluid inside the neutron star, varying according to different density regimes in the neutron star layers. Superfluid neutrons exist in the inner crust where density is  $\approx 4 \times 10^{11} \text{ g cm}^{-3}$  with configuration  $^1S_0$ . Due to the huge density in the core  $> 10^{14} \text{ g cm}^{-3}$  and the nuclear force repulsion between neutrons, the Cooper pairs tend to turn into a more preferable configuration  $^3P_2$ , the core also contains superconducting protons with configuration  $^1S_0$  [11]. When two neutrons are bounded in Cooper pairs, one of the consequences of the BCS is that there exists a *superfluid gap* in analogy to the superconductor gap. In a fermionic system of superfluid neutrons, the Cooper pairs need extra energy to break up they need extra energy, a random small energy would not allow the pairs to break up due to the Pauli exclusion principle. Hence, there is an excitation energy gap for the neutron Cooper pairs to break (see Figure 3.1). The continuous breaking and formation of neutron Cooper pairs occurs while the core is near the critical temperature for the onset of superfluidity, and is referred to as the "PBF" process. This result is increasing the role of the neutron star cooling instantly. Eventually leading to a decrease in the

neutrino emissivity, which in turn decreases the cooling rate, with the neutron star returning to act like regular cooling neutron stars without superfluid effects.

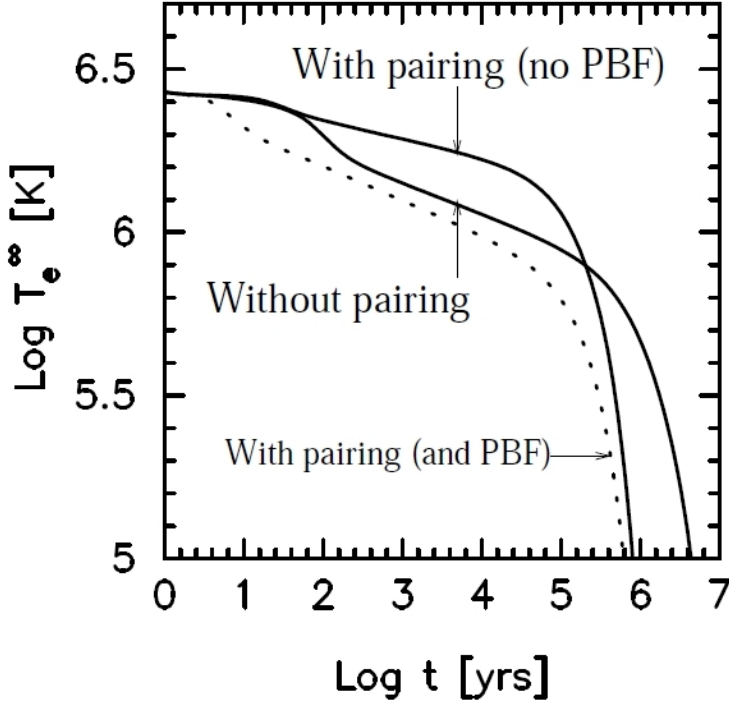


Figure 3.2: The theoretical different cooling curves of a  $1.4 M_{\odot}$  neutron star as a function of time using APR equation of state with envelope of heavy elements. The comparison shows the effect of the nucleon pairing and the the continuous breaking and formation process (PBF) on the cooling curves. The cooling is steeper when nucleon pairing is present along with the PBF process being turned on. Figure from [39].

Shternin et al. analyzed an extra data point produced by two observations<sup>4</sup> in late 2010 observed by Patnaude et al. for the neutron star in Cas A and combined it to the previous observations of Heinke and Ho. Those authors used the non-magnetized carbon atmosphere fitting model with the same fitting parameters in the previous observations, and found a continued decline. The reason proposed for the rapid cooling result of the neutron star in Cas A was enhanced neutrino emission from the core as a result of the continuous breaking and formation of neutron Cooper pairs (i.e. PBF process). Figure 3.2 shows the cooling curves as a function of time and reveals the effect of the pairing and the PBF process on the cooling curves. There is a rapid cooling phase that the neutron star will encounter, at an age somewhere between  $\sim 10^2$  years and  $\sim 10^5$  years. Although the superfluid critical temperature

<sup>4</sup> ObsIDs: 10936 and 12177, from by ACIS-S and telemetered in GRAGED mode, the telemetry mode used by Heinke and Ho

for the  ${}^3\text{P}_2$  neutrons pairing in the neutron star core that would result in the enhanced enutrino emission is uncertain, [Page et al.](#) calculates  $T_C \simeq 0.5 \times 10^9$  K. The pairing critical temperature  $T_C$  is bell shaped as a function of the neutron fermi momentum  $k_F$ . If we assume an isothermal core at temperature  $T$ , hence the the superfluid phase transition for the neutrons will start when the temperature of the core  $T$  reaches the maximum of the critical temperature of  $T_C$ . [Figure 3.3](#) shows that the cooling curves are also highly dependent on the critical temperature  $T_C$  and locates the calculated  $T_C \simeq 0.5 \times 10^9$  K for the neutron star in Cas A [\[40\]](#).

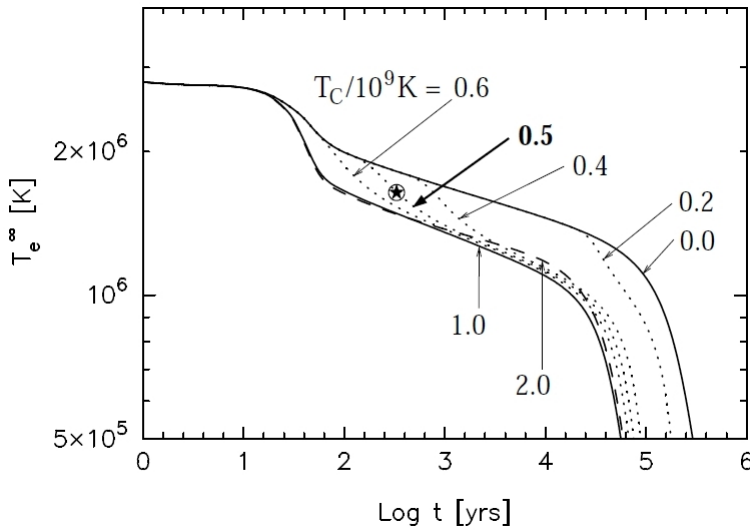


Figure 3.3: The different theoretical cooling curves as a function of time.  $T_2^\infty$  is the redshifted effective temperature of the neutron star. This figure shows that the cooling curves are strongly dependent on the superfluid critical temperature  $T_C$  for the  ${}^3\text{P}_2$  neutrons (in units of  $(10^9$  K). The neutron star is assume to be thermally relaxed and the core is isothermal. Figure from [\[40\]](#).

[Page et al.](#) propose a thermal evolution scenario for the neutron star in Cas A as follows:

- The core of the neutron star has become isothermal at temperature  $T$  a few years after birth ( $10 - 100$  years) and the dominant cooling mechanism was the standard neutrino emission from modified Urca process.
- Once  $T$  reaches the *maximum* superfluid neutron critical temperature, the neutrino emission is enhanced through the continuous formation and breaking of neutron Cooper pairs (PBF process) which becomes a more efficient cooling mechanism than the modified Urca process. The neutrino luminosity from the PBF process is an order of magnitude greater than that from the modified Urca process.

- If the core of the neutron star has reached critical temperature  $T_C$  only recently (at ages of 160 – 300 years), this gives an estimated value of  $T_C \sim 0.5 \times 10^9$  K.

---

## TESTING THE COOLING - *THE NOW WHAT?*

---

### 4.1 RATIONALE

The  $\sim 4\%$  temperature drop from Heinke & Ho [24] discussed in [Section 3.4](#) was inferred from ACIS-S (GRADED mode) observations. In this part, I test the temperature drop over the same 10 years for the neutron star in Cas A using the observations from the other imaging detectors on *Chandra*, HRC-S, HRC-I, ACIS-I and ACIS-S (FAINT mode), to investigate of what level they agree or disagree with the previous result. Several issues relating to the details of the observations and the instrument calibrations can significantly affect the inferred cooling result, since we are testing a small drop of 10-20% in flux over 10 years.

The key point of the analysis is to measure the change of temperature over time inferred by each detector on *Chandra*, as opposed to accurately measure the temperature at each observation. This requires careful consideration of the changes of the detectors' quantum efficiency and effective area over time.

The best-calibrated (because they are the most sensitive and most used) detectors on *Chandra* are the ACIS imaging detectors, which have several known problems that may affect the reliability of the Heinke & Ho measurement. See [Section 2.3.1](#) for more details on the ACIS instrument and these problems; here we summarize them. One of these problems is Charge Transfer Inefficiency (CTI), where a fraction of the charge from a photon is lost as the charge transfers from one pixel to another on the CCD during the readout time of the detector [62], allowing an alteration of the measured energy of the photon. Another issue is event pileup, where the detector reads two photons landing on the same or adjacent pixels within one exposure time as a single photon, resulting in measuring a lower count rate and a higher energy for each photon [10]. Grade migration, caused by either CTI or pileup, is where the pattern of released electrons on the detector is altered from a pattern typical of a single photon (denoted a "good" grade) to a pattern atypical of single photons (a "bad" grade, commonly produced by cosmic rays).

Robert Rutledge has reported <sup>1</sup> that the ACIS-S detector, when operating in GRADED mode, has suffered increasing rates of grade migration during the past ten years, due to radiation damage on the ACIS CCDs causing increased CTI. Data provided in GRADED mode omits all data judged to be “bad” grades from the *Chandra* telemetry stream, so the increased rates of grade migration will lead directly to a (previously uncalibrated) decrease in countrate for GRADED mode data over the *Chandra* lifetime.

Since Cas A is a very bright source, most ACIS data on it has been taken in GRADED mode, and this problem could affect the Cas A neutron star temperature decline result.

Recent discussion with the *Chandra* X-ray Centre calibration team<sup>2</sup> indicates that grade migration on ACIS-S leads to a 2% – 3% drop in countrate over 10 years, which will decrease the size of the Cas A neutron star temperature drop by ~25%. This key point provides a reason to carefully test the temperature drop using other detectors on *Chandra*. The HRC camera is a good candidate since it uses a different detector system than the ACIS CCDs, so should not suffer the same systematic uncertainties (though it may have other problems).

Strong observational confirmation is important to investigate the ACIS-S result. Agreement in the result from different detectors would indicate strong observational confirmation of the current theory behind the rapid cooling of the neutron star in Cas A of a superfluid core.

## 4.2 METHODS

The analysis was conducted using the *Chandra* Interactive Analysis of Observations (CIAO) 4.3 along with the Calibration Database (CALDB) 4.4.6. Although CALDB v. 4.4.8 is now more recent version, there are no significant changes to the relevant files used for this analysis. Specifically, there are no changes to estimates of how the quantum efficiency of the detectors change over time. This work focuses on measuring the change of the temperature over time in each detector, rather than accurate absolute measurements of the temperature from each observation. Below we describe details of the analysis for each detector.

---

<sup>1</sup> Talk at the Institute for Nuclear Theory conference on astrophysical transients, <http://www.int.washington.edu/PROGRAMS/11-2b/>

<sup>2</sup> Discussions with Larry David, Vinay Kashyap, and Jeremy Drake from the *Chandra* calibration team

#### 4.2.1 HRC-S:

The Cas A supernova remnant was observed by the *Chandra* HRC-S camera in September 1999, October 2000, and September 2001, and then five long exposures in March 2009. Table 4.4 lists the ObsIDs considered in my analysis with their exposure times. The HRC-S data are good candidates to compare with the ACIS-S observations, since the HRC-S observations place the neutron star near the optical axis of the telescope with  $\theta_{\text{off-axis}} < 0.5'$ , reducing systematic effects of off-axis angle. Most importantly –apart from ObsID 172 in 1999 of only 9.5 ks– these are deep observations of 50 to 130 ks, providing sufficient statistics for a clear result. All observations are taken without the grating inserted. Since ObsIDs 10227, 10228, 10229, 10698 and 10892 were taken within ten days in 2009, I merged them into a single observation for the purposes of this analysis. Three other HRC-S ObsIDs were not considered here because the supernova remnant is at very large offset angles, and thus totally out of focus. I used the processed event-2 files from the public *Chandra* Observation Catalogue <sup>3</sup>.

The source extraction region is a circle and the background region is an annulus. The background-subtracted source counts was computed using the FUNTOOLS script <sup>4</sup> and then divided by the *live time* to compute the countrates.

Since the spectral energy resolution of HRC-S is almost negligible, no significant spectral information can be extracted from HRC-S observations. Therefore our approach is to calculate, for each observation, a set of conversion factors between observed countrate and neutron star temperature, using a simulated spectrum (verified by successful fitting to ACIS observations) and the relevant response files for that observation. Then we use the observed countrates to calculate the neutron star temperature at each epoch. The multiplication of the telescope/filter/detector areas or the *effective area* [cm<sup>2</sup>] and the quantum efficiency (QE) of the detector as a function of energy [counts/photon] gives the Auxiliary Response File (ARF) matrix [cm<sup>2</sup> counts/photon]. The correct ARF has been generated for each HRC-S observation using the CIAO tool `mkarf`. The Redistribution Matrix File (RMF) is the other required response file, giving the fraction of events at a given incident energy to be recorded at any detector pulse height amplitude (PHA) value. The poor spectral resolution of HRC-S means that this matrix has very substantial terms far off the diagonal. A simple RMF file for HRC-S was released by the CXC in 2010, which we use here, but it is not expected to be of high accuracy ([http://cxc.harvard.edu/ciao4.4/why/hrc\\_rmf.html](http://cxc.harvard.edu/ciao4.4/why/hrc_rmf.html)). However, the choice of RMF is not likely to have a strong impact on this

<sup>3</sup> *Chandra* Observation Catalogue is available on: <http://cda.harvard.edu/chaser/>

<sup>4</sup> FUNTOOLS script written by John Roll: <https://www.cfa.harvard.edu/~john/funtools/ds9.html>

work, since we only use the total countrate of HRC data, rather than attempting spectral fitting.

Using XSPEC v. 12.7.0 [2], the best fit values from the ACIS-S spectral fitting [58] with the nonmagnetized carbon atmosphere, scattering of soft X-rays by interstellar dust [49] and the Tuebingen-Boulder model for absorption by interstellar gas & dust [65], we created a table of temperatures corresponding to different countrates at each epoch. Thus, I generated a model-predicted countrate, corresponding to the *real* measured countrate within  $< 1\%$ , to calculate the temperature for each HRC-S observation. I allowed only the temperature of the neutron star to vary (as physically expected), fixing the other parameters at their known or best measured values from ACIS spectra [58]; the distance at  $d = 3.4$  kpc, the radius  $R_{\text{NS}} = 10.19$  km, the mass at  $M_{\text{NS}} = 1.61M_{\odot}$ , and the interstellar absorption  $n_{\text{H}} = 1.734 \times 10^{22} \text{ cm}^{-2}$ .

Deep ACIS-S observations of the sky area around the Cas A neutron star reveal strong variability of filaments of the supernova remnant over time [44]. Some of these filaments cross the neutron star from our perspective. Figure 4.1 shows filaments growing stronger, and perhaps crossing over the neutron star, in the late observations of 2009. It is not clear whether the part of the filament lying across the neutron star is brightening as much as the neighbouring parts of the filament. If the filament lying across the neutron star is not brightening, then the brightening of filaments in the background region will have the effect of making the neutron star appear fainter. However, if the filaments lying across the neutron star brighten more than other filaments, the opposite effect will be seen. I attempted to identify the behaviour of the filaments by making images of the area around the neutron star in hard energy bands: 5 – 6 keV, 5 – 7 keV and 7 – 8 keV. However, the neutron star still contributed counts in these bands, so the behaviour of the filaments across the neutron star was difficult to determine. We tentatively assume that the filament crossing over the neutron star has the same surface brightness as nearby filaments.

To test the significance of choosing different regions on the measured countrates and the inferred temperatures, several choices have been considered for the source and background extraction regions. The smallest reasonable region that ensures a minimum 90% of the enclosed point source energy is a circle with radius of 1.3" (10 pixels) as Figure 4.2 suggests along with an annulus background of radii 2"-3.3" (referred to as Case I, hereafter).

This source extraction region is smaller than the region considered by Heinke and Ho. Larger choices of source region were also considered, with radii of either 3" or 1.97", the latter used by Heinke and Ho. For the background region, several choices of annuli have been considered, the smallest reasonable choice is a (2" – 3.3") annulus and larger choice

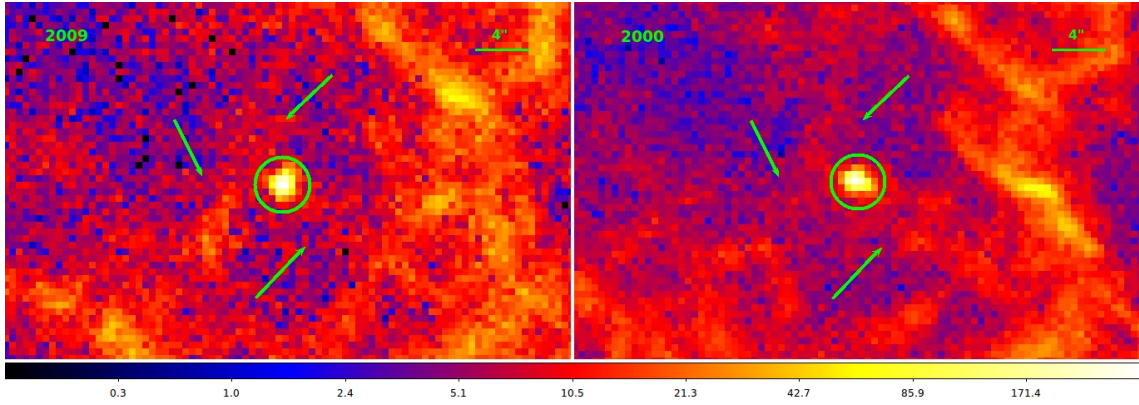


Figure 4.1: Comparison between two deep ACIS-S observations for the neutron star in Cas A. **Left:** ObsID 10935 in 2009 with exposure of 25 ks, showing strong filamentary structure in the vicinity of the neutron star. **Right:** ObsID 114 taken in 2000 with a 50 ks exposure, shows that these filaments were less bright. The simplest assumption is that the filamentary structure crosses the neutron star as well as the background. It is very difficult to reach to a robust conclusion about the exact behaviour of these filaments.

of (5" – 8") annulus was considered. Because the latter region is large and extends further away from the neutron star, the filament variability is more significant in this region, therefore we created a background region of this area excluding the filaments crossing the annulus (see Figure 4.1). To keep comparisons consistent, the regions showing bright filaments in some observations were excluded in all observations. The details of these regions are:

```
# Region file format: CIAO version 1.0
circle(23:23:27.927,+58:48:42.21,0.05') #Source
annulus(23:23:27.927,+58:48:42.21,0.0833334',0.133333') #Background
-ellipse(23:23:28.553,+58:48:37.68,0.0683226',0.0221432',311.386) #
  Background (Filament 1 to extract)
-ellipse(23:23:27.197,+58:48:38.73,0.0683226',0.0221432',234.827) #
  Background (Filament 2 to extract)
```

Finally, a (2.5" – 3.9") background annulus was also considered, the same background region used by Heinke and Ho. The countrates were measured using the counts computed by the FUNTOOLS script <sup>5</sup> and the *live time* of the observation.

#### 4.2.2 HRC-I:

Nineteen observations of Cas A were made using the HRC-I, all of them on-axis ( $\theta_{\text{off-axis}} < 0.5'$ ), spaced between 2000 and 2010. However, with

<sup>5</sup> FUNTOOLS script written by John Roll: <https://www.cfa.harvard.edu/~john/funtools/ds9.html>

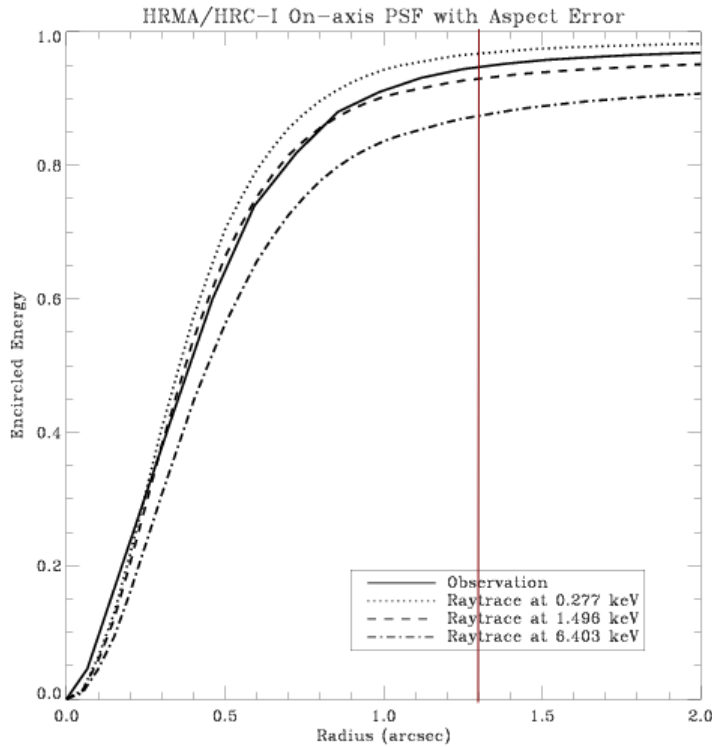


Figure 4.2: HRMA/HRC-I point spread function (PSF) as a function of energy enclosed for on-axis observations. The red vertical line corresponds to the 1.3" radius of the source region considered in the analysis to ensure a minimum  $\sim 90\%$  of the source energy at 1.5 keV is enclosed. Source: Chandra X-ray Observatory Proposer's Guide.

the exception of ObsID 11240 and ObsID 12059 which are of  $\sim 13$  ks exposure time, most of the HRC-I observations are only around 5 ks. We used the same analysis method as in the HRC-S analysis, using the HRC-I response matrix (`hrcid1999-07-22rmfN0002.fits`) generated by the *Chandra* X-ray Center in Dec 2009. The proper ARF files were computed for each observation using `mkarf`, and used together with the RMF to simulate HRC-I spectra and determine the countrate-temperature conversion. The countrates of some HRC-I observations are high ( $> 185$  cts/s) which may have caused telemetry saturation.

[Table 4.1](#) gives the observations, exposure times, off-axis angles, countrates, and inferred temperatures.

#### 4.2.3 ACIS-I:

All observations from the ACIS-I detector were analysed. Although these are more frequent, with 23 ACIS-I observations between 2000 and 2009, they are significantly shorter in exposure time, with average lengths of 1.7 ks. All observations were taken on chip I<sub>3</sub>, except for ObsID 223 on chip I<sub>0</sub>, ObsID 224 on chip I<sub>1</sub> and ObsID 225 on chip I<sub>2</sub>. The aim point of the ACIS-I detector is on the corner of the chip I<sub>3</sub> (see chap-

ObsID	Year	Exposure [ks]	Off axis [arcmin]	Countrate [ $\times 10^{-2} \text{ s}^{-1}$ ]	$T_6$ [ $\times 10^6 \text{ K}$ ]
1549	2001.0	4.9	0.11	3.28	$2.101^{\pm 0.030}$
1550	2001.5	4.8	0.5	2.98	$2.064^{\pm 0.030}$
2871	2002.1	4.9	0.03	2.80	$2.040^{\pm 0.031}$
2878	2002.6	1.5	0.56	2.20	$1.952^{\pm 0.056}$
3698	2003.2	5.0	0.15	2.17	$1.946^{\pm 0.032}$
3705	2003.8	5.0	0.5	2.76	$2.036^{\pm 0.031}$
5157	2004.8	5.1	0.47	2.74	$2.033^{\pm 0.031}$
5164	2004.2	4.8	0.17	2.62	$2.013^{\pm 0.033}$
6069	2005.8	5.1	0.28	3.20	$2.093^{\pm 0.030}$
6083	2005.8	5.1	0.48	3.06	$2.080^{\pm 0.030}$
6739	2006.2	5.0	0.17	3.00	$2.060^{\pm 0.031}$
6746	2006.8	5.0	0.49	2.96	$2.063^{\pm 0.031}$
8370	2007.2	5.0	0.13	2.66	$2.020^{\pm 0.030}$
9700	2008.2	5.0	0.2	3.38	$2.112^{\pm 0.030}$
11240	2009.9	12.9	0.23	2.79	$2.040^{\pm 0.019}$
12057	2009.9	10.9	0.23	2.49	$1.997^{\pm 0.022}$
12058	2009.9	9.2	0.22	2.66	$1.998^{\pm 0.047}$
12059	2009.9	12.8	0.23	2.31	$1.970^{\pm 0.020}$
11955	2010.3	9.5	0.28	2.67	$2.021^{\pm 0.023}$

Table 4.1: The derived HRC-I temperatures from the best fit values of the non-magnetized Carbon atmosphere ACIS-S spectrum. The best fit for the drop is  $8.9 \pm -1.7\%$  over 10 years with very poor  $\chi^2 = 40$  for 17 d.o.f.

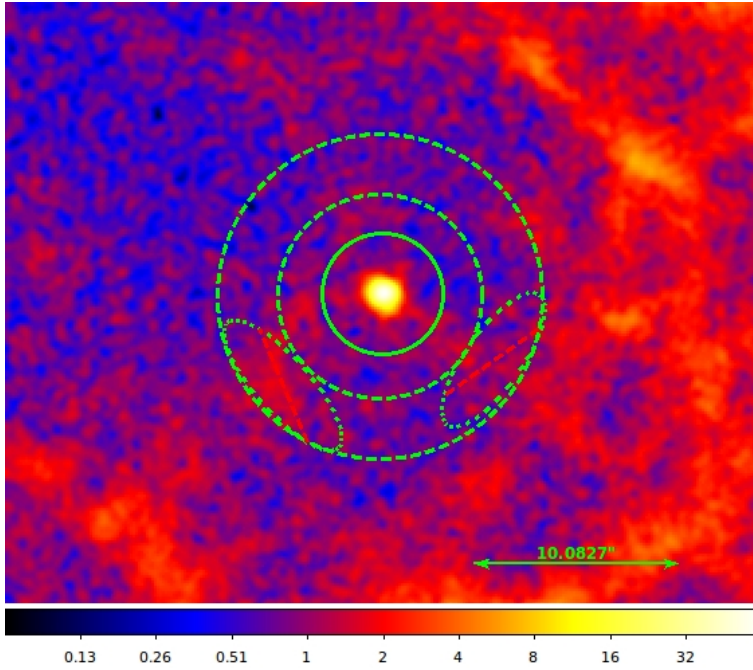


Figure 4.3: **Dashed line** regions represents the background considered. The two ellipses are the excluded regions with the filament activity. Annulus is 5"-8" and the **solid line** region is the source with radius of 3". 2009 HRC-S ObsID 10227 image of Cas A NS.

ter 2 for details). These ACIS-I observations were aimed to focus more on the supernova remnant than the neutron star, thus preferring to place the whole supernova remnant on one chip. This places the neutron star at large off-axis angles (see Figure 4.5), with a considerable effect on the PSF, smearing the point source significantly; see Figure 4.6. Providing accurate calibration information for every position on the ACIS-I chip at different off-axis angles would take too much time to be feasible.

I used larger source extraction regions of 4.2" (8.5 pixels) radii, to make sure that the extraction region of the source contains most of the smeared point-spread function. The background used is an annulus with radii (6.3" – 12.5") excluding (in all observations) a region with strong filament structure from the supernova remnant (see Figure 4.4). Different observations have different telescope roll angles that would result in including different filamentary features in background regions.

The detailed region used for ACIS-I observations is:

```
# Region file format: CIAO version 1.0
circle(23:23:27.919,+58:48:42.19,4.182")
annulus(23:23:27.919,+58:48:42,6.32456",12.6491") # background
-box(23:23:26.642,+58:48:42.10,6.765",22.9395",0.00710507) #
background
```

The Cas A neutron star is a bright source, which can cause pileup in the detector (Section 2.3.1). Extracted spectra of all observations were binned at minimum 25 counts per bin. Assuming all ACIS-I observa-

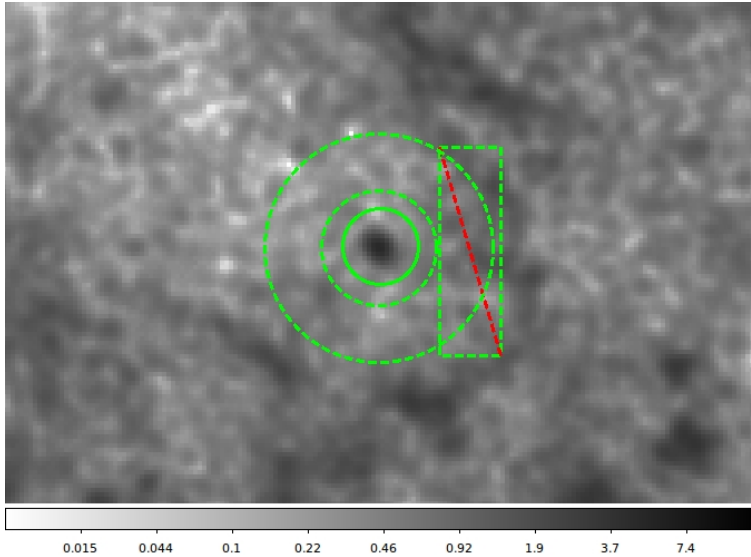


Figure 4.4: ObsID 9698 is shown. **Solid line** region is the source with 4.2'' radius. **Dashed line** region is the background region. The red dashed line is excluded region from background. These regions are the fixed for all ACIS-I analysis.

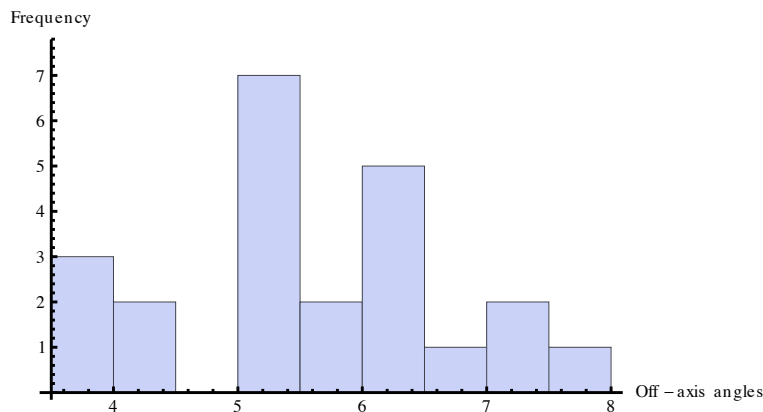


Figure 4.5: Histogram of the number of observations at different off-axis angles (in arcmin) using ACIS-I detector.

tions suffer from similar levels of pileup, a pileup model [10] was used to fit the extracted ACIS-I spectra. The grade migration parameter  $\alpha$  in the pileup model in ACIS-I may be different from ACIS-S. We fixed  $\alpha = 0.5$ , the nominal best value of Davis [10], which is higher than used by Heinke and Ho where the authors allowed  $\alpha$  to vary, finding 0.24 to 0.27 for different frame times. Varying  $\alpha$  had little effect. All ACIS-I observations were taken with a 3.24 s frame time, except ObsID 10624 at 3.04 s frame time (due to only turning on one chip). In the pileup model, the maximum number of photons is fixed to 5 and the PSF fraction to 0.95 in fitting all observations.

Table 4.2 gives the observations, exposure times, off-axis angles, countrates, and inferred temperatures.

ObsID	Year	Exposure [ks]	Off axis [arcmin]	Countrate [ $\times 10^{-2} \text{ s}^{-1}$ ]	$T_6$ [ $\times 10^6 \text{ K}$ ]
223	2000.2	0.8	7.6	4.94	$2.034^{\pm 0.104}$
224	2000.2	1.0	6.6	5.72	$2.020^{\pm 0.080}$
225	2000.2	1.0	7.2	7.23	$2.131^{\pm 0.080}$
226	2000.2	2.7	3.9	9.59	$2.140^{\pm 0.042}$
233	2000.2	1.3	5.4	10.60	$2.189^{\pm 0.065}$
234	2000.2	1.3	7.2	7.89	$2.221^{\pm 0.071}$
235	2000.2	1.3	6.2	9.12	$2.247^{\pm 0.068}$
194	2000.4	3.4	4.3	8.03	$2.067^{\pm 0.040}$
1545	2001.0	1.5	3.6	6.66	$2.054^{\pm 0.062}$
1546	2001.5	1.4	4.0	8.22	$2.097^{\pm 0.061}$
2869	2002.1	1.4	3.6	6.68	$2.043^{\pm 0.064}$
2876	2002.7	1.4	5.4	8.21	$2.139^{\pm 0.062}$
3696	2003.2	1.6	5.3	8.07	$2.114^{\pm 0.056}$
3703	2003.8	1.5	6.2	8.19	$2.209^{\pm 0.060}$
5162	2004.2	1.4	5.2	7.69	$2.148^{\pm 0.061}$
5155	2004.8	1.6	6.2	7.26	$2.153^{\pm 0.061}$
6067	2005.3	1.7	5.7	9.13	$1.937^{\pm 0.040}$
6081	2005.8	1.7	6.2	7.70	$2.019^{\pm 0.048}$
6737	2006.2	1.7	5.4	6.23	$1.812^{\pm 0.043}$
6744	2006.8	1.7	6.2	6.26	$2.099^{\pm 0.061}$
8368	2007.2	1.7	5.1	5.34	$1.963^{\pm 0.064}$
9698	2008.2	1.8	5.4	6.67	$2.046^{\pm 0.056}$
10642	2009.4	1.8	5.7	6.54	$1.966^{\pm 0.049}$

Table 4.2: The derived ACIS-I temperatures from the best fit values of the non-magnetized Carbon atmosphere ACIS-S spectrum. The best fit for the drop is  $8.9 \pm -1.7\%$  over 10 years, with very poor  $\chi^2 = 60$  for 21 d.o.f.

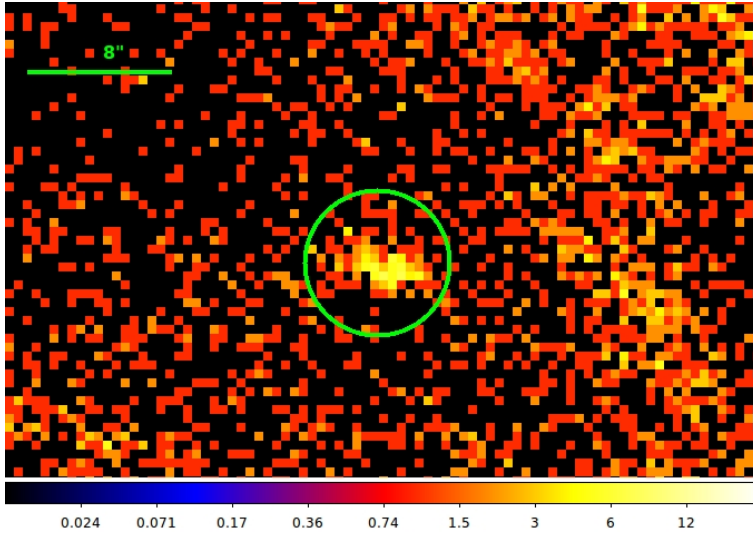


Figure 4.6: The smearing of the image of the neutron star in ACIS-I ObsID 2876 as a result of its  $5.4'$  off-axis angle.

#### 4.2.4 ACIS-S, FAINT Mode

Finally, ACIS-S FAINT observations were also analysed using the same technique used with ACIS-I. These nineteen observations are more distributed in time than the HRC-S observations and do not suffer from large off-axis angles. Most of the ACIS-S FAINT observations have  $\theta_{\text{off-axis}} \sim 2.5'$ , similar to the ACIS-S GRADED mode observations (this centers the supernova remnant on the S3 chip). However, most of these observations have short exposure times around 1 ks, leading to large uncertainties in the final countrates. ObsID 6690 is the only observation was taken in subarray mode and hence it was excluded from the analysis to keep comparisons consistent. The ACIS-S FAINT observations have high countrate ( $> 320$  cts/s) in 100 seconds binned light curve which could lead to concern about telemetry saturation. ObsIDs 1547, 1548, 2877, 8369 and 10643 may suffer from dropped frametime in the live exposure time (reported in V&V reports from CXO). ObsID 9699 shows a significantly lower inferred countrate ( $0.047 \pm 0.005$  cts/s) and measured temperature ( $1.814 \pm 0.037 \times 10^6$  K), the reason for this is unclear. Table 4.3 gives the observations, exposure times, off-axis angles, countrates, and inferred temperatures.

### 4.3 RESULTS AND DISCUSSION

#### 4.3.1 HRC-S:

Chi-squared fitting to countrates and temperatures over time was performed using QDP<sup>6</sup> for a  $y = ax + b$  fit, with  $1 - \sigma$  errors. To get an idea

<sup>6</sup> <http://heasarc.gsfc.nasa.gov/docs/software/ftools/others/qdp/node3.html>

ObsID	Year	Exposure [ks]	Off axis [arcmin]	Countrate [ $\times 10^{-2} \text{ s}^{-1}$ ]	$T_6$ [ $\times 10^6 \text{ K}$ ]
230	2000.2	2.1	2.6	1.91	$2.090^{\pm 0.040}$
236	2000.2	1.0	3.1	2.86	$2.161^{\pm 0.062}$
237	2000.2	1.0	4.4	2.78	$2.162^{\pm 0.060}$
198	2000.4	2.5	0.9	1.53	$2.090^{\pm 0.032}$
1547	2001.0	1.1	2.2	2.48	$2.140^{\pm 0.053}$
1548	2001.5	1.1	2.7	2.69	$2.047^{\pm 0.055}$
2870	2002.1	1.8	2.4	2.61	$2.030^{\pm 0.053}$
2877	2002.7	1.1	3.0	2.78	$2.018^{\pm 0.050}$
3697	2003.2	1.2	2.6	2.39	$2.088^{\pm 0.051}$
3704	2003.8	1.2	2.6	2.45	$2.081^{\pm 0.056}$
5163	2004.2	1.1	2.6	2.59	$2.089^{\pm 0.050}$
5156	2004.8	1.1	2.5	2.68	$2.089^{\pm 0.054}$
6068	2005.3	1.2	2.6	2.45	$2.041^{\pm 0.050}$
6082	2005.8	1.2	2.6	2.43	$2.058^{\pm 0.022}$
6738	2006.2	1.2	2.6	2.24	$2.095^{\pm 0.047}$
6745	2006.8	1.2	2.7	2.48	$2.053^{\pm 0.051}$
8369	2007.2	1.3	2.6	2.25	$2.132^{\pm 0.048}$
9699	2008.2	2.2	2.6	2.04	$1.814^{\pm 0.037}$
10643	2009.4	1.3	2.4	2.27	$2.074^{\pm 0.047}$

Table 4.3: The derived ACIS-S (FAINT) temperatures from the best fit values of the non-magnetized Carbon atmosphere ACIS-S spectrum. The best fit for the drop in temperature is  $8.9 \pm -1.7\%$  over 10 years, with very poor  $\chi^2 = 9.3$  for 16 d.o.f.

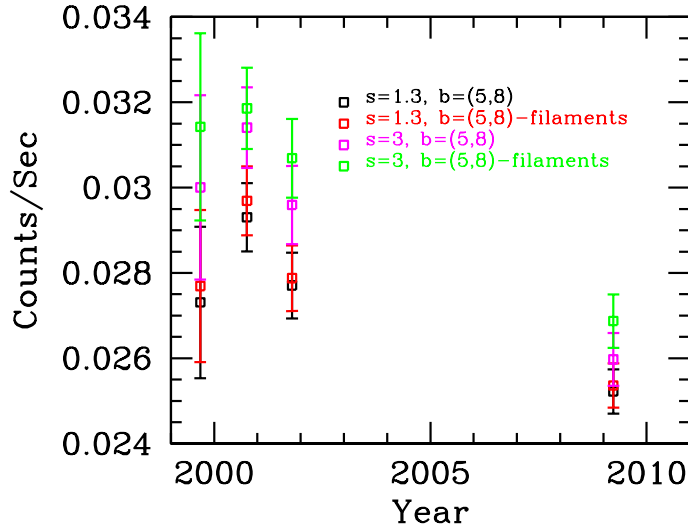


Figure 4.7: Inferred temperatures ( $1 - \sigma$ ) from HRC-S countrates, assuming the carbon atmosphere model spectrum, using a large background (b) annulus. Different choices of source size (s), and choices of whether regions containing bright supernova remnant filaments are removed from the background annulus, are compared. Different choices of source region produce a larger countrate variation than whether bright filaments are excluded from the background annulus.

about the effect of the filaments in the background and crossing the neutron star, I compared the countrate drops using a large background region with filaments excluded, and two choices of source region (radius 1.3" and 3"). Figure 4.7 shows that the effect of choosing different regions for the source is more significant than choosing different regions for the background with or without excluding the filaments, this may infer a strong filamentary structure crossing the neutron star.

The linear fitting for the decline in the HRC-S count rate in Case I gives a countrate drop of  $12.2^{+2.8}_{-2.8}\%$  ( $1 - \sigma$  errors) over 10 years. Case II is not very different, where the decline is  $12.7^{+2.8}_{-2.8}\%$ . In Case III it is slightly higher at  $14.3^{+2.7}_{-2.7}\%$  and Case IV is  $15.4^{+2.7}_{-2.7}\%$ . Table 4.4 summarizes all the HRC-S results for the different choices of extraction and background regions, the measured countrate and the inferred temperatures.

The early 1999 HRC-S observation is significantly lower in exposure time than any of the later HRC-S observations, and therefore it has the

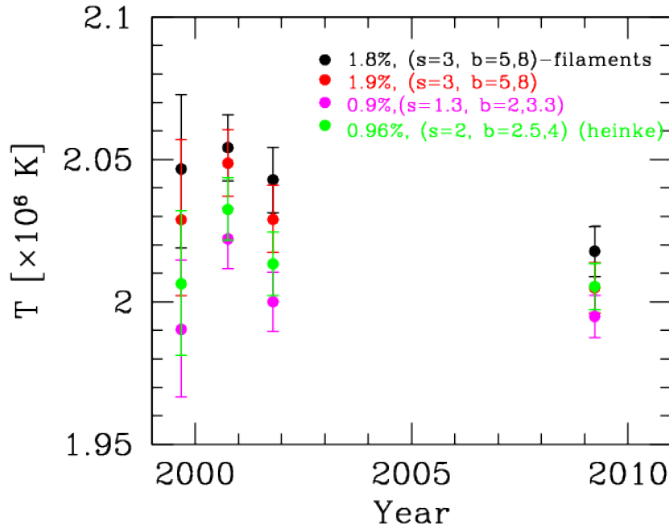


Figure 4.8: Inferred temperatures ( $1 - \sigma$ ) from HRC-S countrates, assuming the carbon atmosphere model spectrum, with different choices of source (s) and background (b) extraction regions. The temperature drop ranges from  $0.9^{+0.6\%}_{-0.6\%} - 1.9^{+0.7\%}_{-0.7\%}$  within  $1 - \sigma$  level with  $\chi^2=8.3$  for 6 d.o.f

largest errorbars. Excluding this observation from fitting increases the decline in countrate by 1.5%, which is less than the  $1 - \sigma$  error.

The current drop in QE released in the calibration of HRC-S is thought to be  $0.75 \pm 0.19\%/year$ ,<sup>7</sup>. This suggests that the actual drop in countrate is  $4.2^{+2.8\%}_{-2.8\%}$ . However discussion with *Chandra* HRC calibration team<sup>8</sup> suggests that in fact the current QE drop in HRC-S may be overestimated, and it might be in fact as low as 5%/10 years, which will raise the drop in countrate to  $7.2^{+2.8\%}_{-2.8\%}$ .

Modelling HRC-S countrate with simulated spectra to infer the decline in temperature indicates only a marginal drop in temperature. The inferred drop in temperatures for different reasonable choices of source and background regions gives a range of possible temperature declines. Cases I and II shows only a marginal decline of  $0.9^{+0.6\%}_{-0.6\%}$ , with  $\chi^2 = 8.3$  for 6 degrees of freedom giving a reduced- $\chi^2 \sim 1.4$ . When increasing the source and background regions reasonably, the inferred drop goes slightly higher to  $1.9^{+0.7\%}_{-0.7\%}$  and  $1.8^{+0.7\%}_{-0.7\%}$  for cases III and IV respectively

<sup>7</sup> <http://cxc.cfa.harvard.edu/cal/Hrc/Monitor/index.html>

<sup>8</sup> Discussions with Larry David and Vinay Kashyap.

ObsID	Year	Exposure [ks]	Count Rate [ $\times 10^{-2}$ cts/s]	$T_{\text{eff}}$ [ $\times 10^6$ K]
Case I				
172	1999.7	9.36	$2.7058^{\pm 0.1797}$	$1.990^{\pm 0.024}$
1857	2000.8	48.44	$2.9299^{\pm 0.0812}$	$2.022^{\pm 0.010}$
1038	2001.8	49.98	$2.7417^{\pm 0.0777}$	$2.000^{\pm 0.010}$
Merged	2009.2	484.35	$2.5271^{\pm 0.0523}$	$1.994^{\pm 0.007}$
Case II				
172	1999.7	9.36	$2.8274^{\pm 0.1942}$	$2.006^{\pm 0.025}$
1857	2000.8	48.44	$3.0100^{\pm 0.0868}$	$2.032^{\pm 0.011}$
1038	2001.8	49.98	$2.8398^{\pm 0.0834}$	$2.013^{\pm 0.011}$
Merged	2009.2	484.35	$2.6005^{\pm 0.0565}$	$2.005^{\pm 0.008}$
Case III				
172	1999.7	9.36	$3.0005^{\pm 0.2160}$	$2.028^{\pm 0.028}$
1857	2000.8	48.44	$3.1405^{\pm 0.0945}$	$2.048^{\pm 0.011}$
1038	2001.8	49.98	$2.9592^{\pm 0.0916}$	$2.028^{\pm 0.011}$
Merged	2009.2	484.35	$2.5974^{\pm 0.0620}$	$2.004^{\pm 0.008}$
Case IV				
172	1999.7	9.36	$3.1424^{\pm 0.2192}$	$2.046^{\pm 0.027}$
1857	2000.8	48.44	$3.1858^{\pm 0.0954}$	$2.054^{\pm 0.011}$
1038	2001.8	49.98	$3.0690^{\pm 0.0922}$	$2.042^{\pm 0.011}$
Merged	2009.2	484.35	$2.6872^{\pm 0.0625}$	$2.017^{\pm 0.008}$

Table 4.4: The inferred HRC-S temperatures computed from the countrates, using appropriate responses and assuming a simulated carbon atmosphere spectrum, for different choices of source and background region. The radii of the different cases are: **Case I**: Source= 1.3", background= 2"-3.3", **Case II**: Source= 1.97", background= 2.5"- 3.9", **Case III**: Source= 3", background= 5"- 8" and **Case IV**: Source= 3", background= 5"- 8" with filaments in [Figure 4.3](#) excluded.

within  $1 - \sigma$  errors (see [Figure 4.8](#)). The fact that cases III and IV use background regions large enough to have significant effects from the filamentary structure of the supernova remnant, and our poor understanding about the behaviour of those filaments, raises concern about accepting these inferred drops. Therefore, I assume that cases I and II are more reliable than cases III and IV.

Reconciling the temperature drops over 10 years measured by HRC-S ( $0.9^{+0.6}_{-0.6}\% - 1.9^{+0.7}_{-0.7}\%$ ) and ACIS-S ( $3.6^{+0.6}_{-0.6}\%$ ) might be done by addressing a few points. On the HRC-S side the microchannel plate loses efficiency with the total incident X-ray flux at a particular location on it. Thus the change in the position of the aimpoint can affect the inferred drop in countrates and temperatures, by exposing a new, less damaged portion of the microchannel plate, although it is not known quantitatively the effect of this change. This reason, along with the possibly overestimated 8% QE drop would work to result in a lower than expected drop in countrate and inferred temperature. Therefore, these issues with HRC-S suggest that the actual drop in temperature and countrate may be higher than inferred. On the other hand, the (previously uncalibrated) 3% drop in QE of the S3 chip on ACIS-S in GRADED mode (see above) leads to a lower inferred drop in temperature. The effect can be estimated to lower the temperature drop to 2.8% over 10 years, instead of 3.6%. Another interesting comparison is in the countrate space, where I directly measured the countrate drop from ACIS-S GRADED observations, the same considered in [Heinke and Ho](#) and resulted in a 13% drop. When taking into account the drop in the QE of ACIS-S S3 chip of 2% – 3% this gives a  $\sim 10\%$  drop in countrate, which makes it unlikely consistent with the  $\sim 8\%$  drop (the linear fitting for decline in countrates is 15% and subtracting  $\sim 7\%$  drop in HRC-S QE), in HRC-S countrates.

#### 4.3.2 *Other detectors:*

The temperature measurements inferred from ACIS-I are highly scattered and cannot give strong confirmation, due to the fact that most of them are off-axis observations. The temperatures measured from ACIS-I when linearly fitted, gives a decline of  $8.9^{+1.7}_{-1.7}\%$  over 10 years (with  $1 - \sigma$  errors) (see [Figure 4.9](#)). The linear fit is poor with  $\chi^2 = 60$  for 21 degrees of freedom. Observations may suffer from telemetry saturation, especially these with countrates  $> 230$  cts/s, for a 100 seconds binned light curve. ObsIDs (2869, 2876, 8368) may suffer from dropped frametime. I also fitted the inferred temperatures after multiplying the errors by a factor of 2.8, to reduce the reduced chi-squared to 1.0. The uncertainty on the drop increases, and the drop in this case is  $8.9^{+3}_{-3}\%$ .

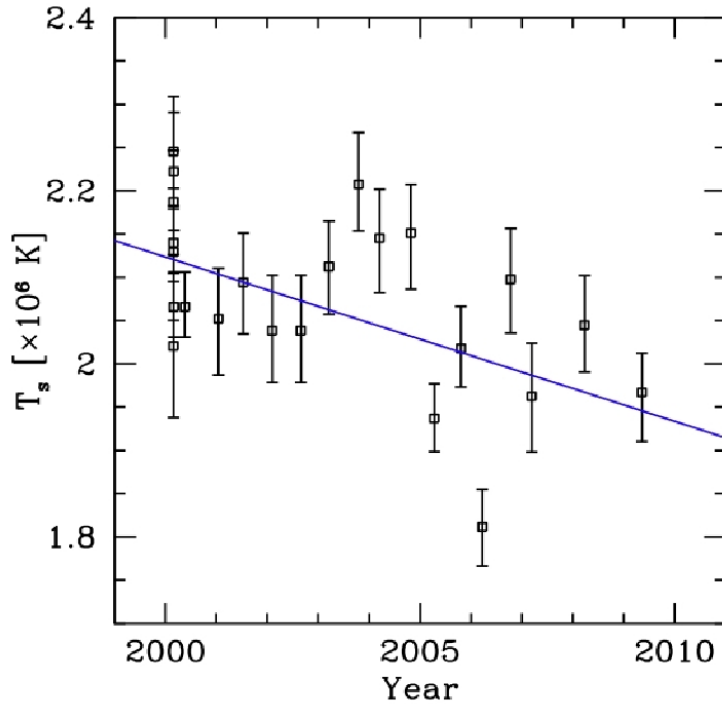


Figure 4.9: The measured temperatures ( $1 - \sigma$ ) from ACIS-I for the neutron star in Cas A, assuming the carbon atmosphere model spectrum. Linear fitting indicates a decline of  $8.9^{+1.7}_{-1.7}\%$  over 10 years (with  $1 - \sigma$  errors). The linear fit is poor with a  $\chi^2$  of 60 for 21 degrees of freedom.

We note that this temperature decline would be much faster than that measured by ACIS-S GRADED observations.

The results from HRC-I suffer from short exposure times and the poor spectral resolution of HRC-I, which cause large errorbars and highly scattered inferred temperature values. Linearly fitting the temperature decline gives a temperature drop of  $2.0^{+1.0}_{-1.0}\%$ . Although this result is consistent with that from ACIS-S GRADED observations, the linear fit to the temperatures gives a poor fit of  $\chi^2 = 40$  for 17 degrees of freedom. Also I did the fitting for the inferred temperature after multiplying the errors by a factor of 2.8, to reduce the reduced chi-squared to 1.0. This increases the uncertainty on the drop, to be  $2^{+2.8}_{-2.8}\%$  over 10 years, which suggests that the inferred result from HRC-I is not significant.

(see [Figure 4.10](#)).

Finally, ACIS-S FAINT observations suffer from strong telemetry overloading in the detector, because Cas A is a very bright source.

The analysis infers a drop of  $1.5^{+2.0}_{-2.0}\%$  (see [Figure 4.11](#)), consistent with the ACIS-S GRADED result, with a linear fit of  $\chi^2 = 9.3$  for 16 degrees of freedom.

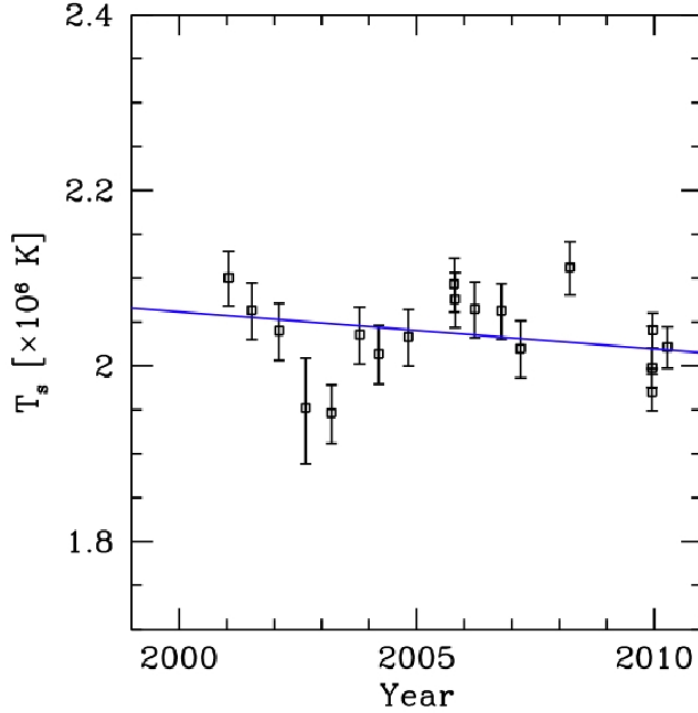


Figure 4.10: Inferred temperatures ( $1 - \sigma$ ) from HRC-I countrates, assuming the carbon atmosphere model spectrum. Linear fitting indicates a decline of  $2.0^{+1.0}_{-1.0}\%$  over 10 years (with  $1 - \sigma$  errors). The linear fit is poor with  $\chi^2$  of 40 for 17 degrees of freedom.

#### 4.4 CONCLUSION

Of all the analysed observations by *Chandra* cameras, HRC-S provides the best instrument to compare with ACIS-S GRADED result. However, the 1% – 1.9% range for the temperature drop inferred from HRC-S is significantly less than that inferred from ACIS-S GRADED observations. The ACIS-S data are known to have suffered from previously uncalibrated grade migration, which we expect to have caused a 2% – 3% decline in QE. Thus, our estimate of the actual drop in temperature from the ACIS-S GRADED data is decreased from 3.6% to 2.8%. The QE of HRC-S might be overestimated which would result in a lower temperature drop inferred by this detector. The results inferred from the observations by the rest of *Chandra* instruments provide a wide range of uncertainties. The ACIS-I observations are mostly affected by being at large off-axis angles and the fact that calibration of ACIS-I PSF for different off-axis angles at different positions on the detector is almost impossible to achieve. The data quality of HRC-I and ACIS-S FAINT observations are not high because of low exposure times and the poor spectral resolution of HRC-I. Hence at best, these instruments only support cooling of the neutron star in Cas A, however they cannot give

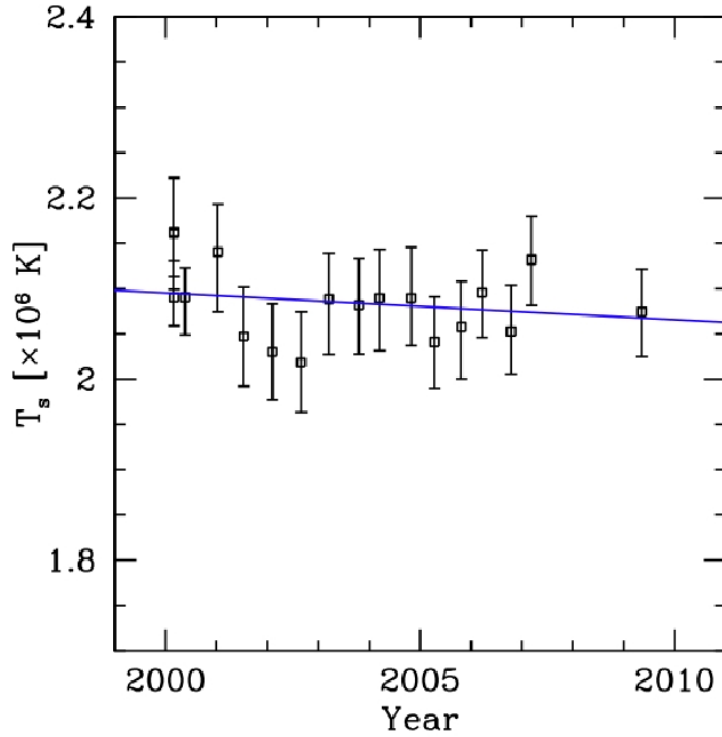


Figure 4.11: The measured temperatures ( $1 - \sigma$ ) from ACIS-S (FAINT) for the neutron star in Cas A, assuming the carbon atmosphere model spectrum. Linear fitting indicates a decline of  $1.5^{+2.0}_{-2.0}\%$  over 10 years (with  $1 - \sigma$  errors). The linear fit is with  $\chi^2$  of 9.3 for 16 degrees of freedom.

an accurate measurement of the drop in temperature of the neutron star over this time period. [Figure 4.12](#) summarizes the different inferred temperature drop over 10 years from all of the cameras on *Chandra*.

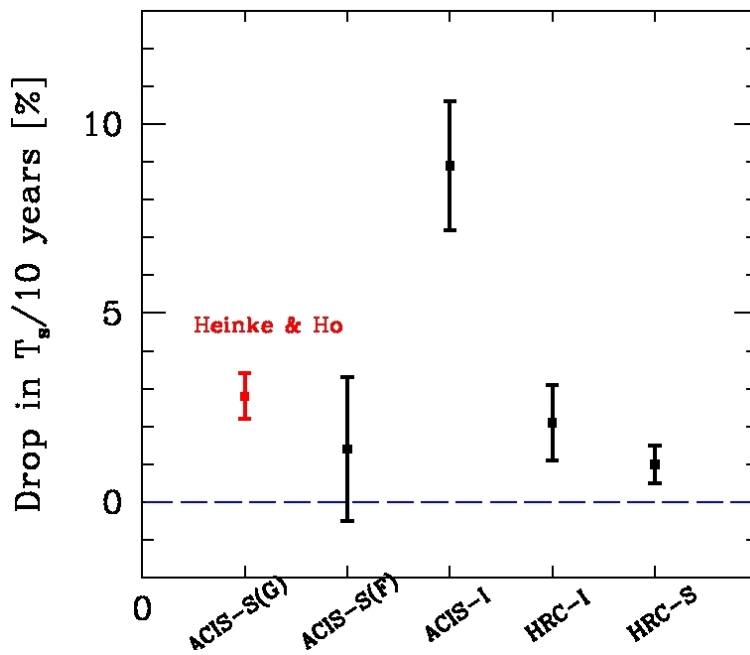


Figure 4.12: The inferred drop in surface temperature of the neutron star in Cas A from all detectors on *Chandra* over 10 years. The ACIS-S GRADED result from [Heinke and Ho](#) has been shifted to 2.8% instead of 3.6%, as suggested by recent *Chandra* calibration efforts. The result from HRC-S puts a lower limit of 1.5% on the cooling. The results from HRC-I, ACIS-I and ACIS-S FAINT observations have various systematic problems, as discussed in the text.

---

## BIBLIOGRAPHY

---

- [1] N. Andersson, K. Glampedakis, W. C. G. Ho, and C. M. Espinoza. Pulsar glitches: The crust is not enough. *ArXiv e-prints*, July 2012.
- [2] K. A. Arnaud. XSPEC: The First Ten Years. In *ASP Conf. Ser. 101: Astronomical Data Analysis Software and Systems V*, page 17, 1996.
- [3] J. Bardeen, L. N. Cooper, and J. R. Schrieffer. Theory of superconductivity. *Phys. Rev.*, 108:1175–1204, Dec 1957. doi: 10.1103/PhysRev.108.1175. URL <http://link.aps.org/doi/10.1103/PhysRev.108.1175>.
- [4] M. G. Baring and A. K. Harding. Radio-Quiet Pulsars with Ultra-strong Magnetic Fields. *Astrophys. J.*, 507:L55–L58, November 1998. doi: 10.1086/311679.
- [5] A. R. Bell. The acceleration of cosmic rays in shock fronts. II. *Mon. Not. R. Astron. Soc.*, 182:443–455, February 1978.
- [6] B. J. Bok and E. F. Reilly. Small Dark Nebulae. *Astrophys. J.*, 105:255, March 1947. doi: 10.1086/144901.
- [7] D. Branch, E. Baron, R. C. Thomas, D. Kasen, W. Li, and A. V. Filippenko. Reading the Spectra of the Most Peculiar Type Ia Supernova 2002cx. *Publications of the Astronomical Society of the Pacific*, 116:903–908, October 2004. doi: 10.1086/425081.
- [8] P. Chang, L. Bildsten, and P. Arras. Diffusive Nuclear Burning of Helium on Neutron Stars. *Astrophys. J.*, 723:719–728, November 2010. doi: 10.1088/0004-637X/723/1/719.
- [9] Leon N. Cooper. Bound electron pairs in a degenerate fermi gas. *Phys. Rev.*, 104:1189–1190, Nov 1956. doi: 10.1103/PhysRev.104.1189. URL <http://link.aps.org/doi/10.1103/PhysRev.104.1189>.
- [10] J. E. Davis. Event Pileup in Charge-coupled Devices. *Astrophys. J.*, 562:575–582, November 2001.
- [11] Ø. Elgarøy, L. Engvik, M. Hjorth-Jensen, and E. Osnes. Triplet pairing of neutrons in  $\beta$ -stable neutron star matter. *Nuclear Physics A*, 607:425–441, February 1996. doi: 10.1016/0375-9474(96)00217-5.
- [12] R. A. Fesen, R. H. Becker, and W. P. Blair. Discovery of fast-moving nitrogen-rich ejecta in the supernova remnant Cassiopeia A. *Astrophys. J.*, 313:378–388, February 1987. doi: 10.1086/164974.

- [13] R. A. Fesen, M. C. Hammell, J. Morse, R. A. Chevalier, K. J. Borkowski, M. A. Dopita, C. L. Gerardy, S. S. Lawrence, J. C. Raymond, and S. van den Bergh. The Expansion Asymmetry and Age of the Cassiopeia A Supernova Remnant. *Astrophys. J.*, 645:283–292, July 2006. doi: 10.1086/504254.
- [14] E. Flowers, M. Ruderman, and P. Sutherland. Neutrino pair emission from finite-temperature neutron superfluid and the cooling of young neutron stars. *Astrophys. J.*, 205:541–544, April 1976. doi: 10.1086/154308.
- [15] W. Forman, C. Jones, L. Cominsky, P. Julien, S. Murray, G. Peters, H. Tananbaum, and R. Giacconi. The fourth Uhuru catalog of X-ray sources. *Astrophys. J.s*, 38:357–412, December 1978. doi: 10.1086/190561.
- [16] H. Friedman, S. W. Lichtman, and E. T. Byram. Photon Counter Measurements of Solar X-Rays and Extreme Ultraviolet Light. *Physical Review*, 83:1025–1030, September 1951. doi: 10.1103/PhysRev.83.1025.
- [17] R. Giacconi, H. Gursky, F. R. Paolini, and B. B. Rossi. Evidence for x Rays From Sources Outside the Solar System. *Physical Review Letters*, 9:439–443, December 1962. doi: 10.1103/PhysRevLett.9.439.
- [18] R. Giacconi, H. Gursky, E. Kellogg, E. Schreier, and H. Tananbaum. Discovery of Periodic X-Ray Pulsations in Centaurus X-3 from UHURU. *Astrophys. J.l*, 167:L67, July 1971. doi: 10.1086/180762.
- [19] O. Y. Gnedin, D. G. Yakovlev, and A. Y. Potekhin. Thermal relaxation in young neutron stars. *Mon. Not. R. Astron. Soc.*, 324:725–736, June 2001. doi: 10.1046/j.1365-8711.2001.04359.x.
- [20] E. V. Gotthelf, B. Koralesky, L. Rudnick, T. W. Jones, U. Hwang, and R. Petre. Chandra Detection of the Forward and Reverse Shocks in Cassiopeia A. *Astrophys. J.l*, 552:L39–L43, May 2001. doi: 10.1086/320250.
- [21] E. V. Gotthelf, R. Perna, and J. P. Halpern. Modeling the Surface X-ray Emission and Viewing Geometry of PSR J0821-4300 in Puppis A. *Astrophys. J.*, 724:1316–1324, December 2010. doi: 10.1088/0004-637X/724/2/1316.
- [22] J. P. Halpern and E. V. Gotthelf. Spin-Down Measurement of PSR J1852+0040 in Kesteven 79: Central Compact Objects as Anti-Magnetars. *Astrophys. J.*, 709:436–446, January 2010. doi: 10.1088/0004-637X/709/1/436.

- [23] J. P. Halpern and E. V. Gotthelf. On the Spin-down and Magnetic Field of the X-ray Pulsar 1E 1207.4-5209. *Astrophys. J.*, 733:L28, June 2011. doi: 10.1088/2041-8205/733/2/L28.
- [24] C. O. Heinke and W. C. G. Ho. Direct Observation of the Cooling of the Cassiopeia A Neutron Star. *Astrophys. J.*, 719:L167–L171, August 2010. doi: 10.1088/2041-8205/719/2/L167.
- [25] W. C. G. Ho and C. O. Heinke. A neutron star with a carbon atmosphere in the Cassiopeia A supernova remnant. *Nature*, 462:71–73, November 2009. doi: 10.1038/nature08525.
- [26] J. P. Hughes, C. E. Rakowski, D. N. Burrows, and P. O. Slane. Nucleosynthesis and Mixing in Cassiopeia A. *Astrophys. J.*, 528:L109–L113, January 2000. doi: 10.1086/312438.
- [27] U. Hwang, A. E. Szymkowiak, R. Petre, and S. S. Holt. Bulk X-Ray Doppler Velocities in the Supernova Remnant Cassiopeia A. *Astrophys. J.*, 560:L175–L179, October 2001. doi: 10.1086/324177.
- [28] U. Hwang, J. M. Laming, C. Badenes, F. Berendse, J. Blondin, D. Cioffi, T. DeLaney, D. Dewey, R. Fesen, K. A. Flanagan, C. L. Fryer, P. Ghavamian, J. P. Hughes, J. A. Morse, P. P. Plucinsky, R. Petre, M. Pohl, L. Rudnick, R. Sankrit, P. O. Slane, R. K. Smith, J. Vink, and J. S. Warren. A Million Second Chandra View of Cassiopeia A. *Astrophys. J.*, 615:L117–L120, November 2004. doi: 10.1086/426186.
- [29] V. M. Kaspi. Grand unification of neutron stars. *Proceedings of the National Academy of Science*, 107:7147–7152, April 2010. doi: 10.1073/pnas.1000812107.
- [30] J. W. Keohane, L. Rudnick, and M. C. Anderson. A Comparison of X-Ray and Radio Emission from the Supernova Remnant Cassiopeia A. *Astrophys. J.*, 466:309, July 1996. doi: 10.1086/177511.
- [31] O. Krause, S. M. Birkmann, T. Usuda, T. Hattori, M. Goto, G. H. Rieke, and K. A. Misselt. The Cassiopeia A Supernova Was of Type IIb. *Science*, 320:1195–, May 2008. doi: 10.1126/science.1155788.
- [32] J. M. Lattimer and M. Prakash. Neutron Star Structure and the Equation of State. *Astrophys. J.*, 550:426–442, March 2001.
- [33] J. M. Lattimer, M. Prakash, C. J. Pethick, and P. Haensel. Direct URCA process in neutron stars. *Physical Review Letters*, 66:2701–2704, May 1991. doi: 10.1103/PhysRevLett.66.2701.
- [34] C. Leong, E. Kellogg, H. Gursky, H. Tananbaum, and R. Giacconi. X-Ray Emission from the Magellanic Clouds Observed by UHURU. *Astrophys. J.*, 170:L67, December 1971. doi: 10.1086/180842.

- [35] C. M. Leung, M. L. Kutner, N. J. Evans, II, and B. A. Rice. Observations and Interpretations of CO Isotope Ratios in Interstellar Molecular Clouds. In *Bulletin of the American Astronomical Society*, volume 17 of *Bulletin of the American Astronomical Society*, page 870, September 1985.
- [36] A. Migdal. Superfluidity and the moments of inertia of nuclei. *Nucl. Phys. A*, 13:655–674, November 1959. doi: 10.1016/0029-5582(59)90264-0.
- [37] S. S. Murray, S. M. Ransom, M. Juda, U. Hwang, and S. S. Holt. Is the Compact Source at the Center of Cassiopeia A Pulsed? *Astrophys. J.*, 566:1039–1044, February 2002. doi: 10.1086/338224.
- [38] R. Negreiros, R. Ruffini, C. L. Bianco, and J. A. Rueda. Cooling of young neutron stars in GRB associated to supernovae. *Astron. Astrophys.*, 540:A12, April 2012. doi: 10.1051/0004-6361/201117006.
- [39] D. Page, J. M. Lattimer, M. Prakash, and A. W. Steiner. Minimal Cooling of Neutron Stars: A New Paradigm. *Astrophys. J.s*, 155: 623–650, December 2004. doi: 10.1086/424844.
- [40] D. Page, M. Prakash, J. M. Lattimer, and A. W. Steiner. Rapid Cooling of the Neutron Star in Cassiopeia A Triggered by Neutron Superfluidity in Dense Matter. *Physical Review Letters*, 106(8):081101, February 2011. doi: 10.1103/PhysRevLett.106.081101.
- [41] F. Palla and S. W. Stahler. The evolution of intermediate-mass protostars. I - Basic results. *Astrophys. J.*, 375:288–299, July 1991. doi: 10.1086/170188.
- [42] D. Patnaude, R. Fesen, J. Vink, and J. M. Laming. The X-ray evolution of Cassiopeia A. In *38th COSPAR Scientific Assembly*, volume 38, page 2727, 2010.
- [43] D. J. Patnaude and R. A. Fesen. Small-Scale X-Ray Variability in the Cassiopeia A Supernova Remnant. *Astron. J.*, 133:147–153, January 2007. doi: 10.1086/509571.
- [44] D. J. Patnaude and R. A. Fesen. Proper Motions and Brightness Variations of Nonthermal X-ray Filaments in the Cassiopeia A Supernova Remnant. *Astrophys. J.*, 697:535–543, May 2009. doi: 10.1088/0004-637X/697/1/535.
- [45] G. G. Pavlov and G. J. M. Luna. A Dedicated Chandra ACIS Observation of the Central Compact Object in the Cassiopeia A Supernova Remnant. *Astrophys. J.*, 703:910–921, September 2009. doi: 10.1088/0004-637X/703/1/910.

- [46] G. G. Pavlov, Y. A. Shibano, V. E. Zavlin, and R. D. Meyer. Neutron Star Atmospheres. In M. A. Alpar, U. Kiziloglu, and J. van Paradijs, editors, *The Lives of the Neutron Stars*, page 71, 1995.
- [47] G. G. Pavlov, V. E. Zavlin, B. Aschenbach, J. Trümper, and D. Sanwal. The Compact Central Object in Cassiopeia A: A Neutron Star with Hot Polar Caps or a Black Hole? *Astrophys. J.*, 531:L53–L56, March 2000. doi: 10.1086/312521.
- [48] C. J. Pethick and V. Thorsson. Neutrino Emission from Dense Matter and Neutron Star Thermal Evolution. In M. A. Alpar, U. Kiziloglu, and J. van Paradijs, editors, *The Lives of the Neutron Stars*, page 121, 1995.
- [49] P. Predehl, E. Costantini, G. Hasinger, and Y. Tanaka. XMM-Newton observation of the galactic centre - evidence against the X-ray reflection nebulae model? *Astronomische Nachrichten*, 324:73–76, 2003.
- [50] J. E. Reed, J. J. Hester, A. C. Fabian, and P. F. Winkler. The Three-dimensional Structure of the Cassiopeia A Supernova Remnant. I. The Spherical Shell. *Astrophys. J.*, 440:706–+, February 1995. doi: 10.1086/175308.
- [51] S. P. Reynolds, K. J. Borkowski, D. A. Green, U. Hwang, I. Harrus, and R. Petre. The Youngest Galactic Supernova Remnant: G1.9+0.3. *Astrophys. J. L.*, 680:L41–L44, June 2008. doi: 10.1086/589570.
- [52] J. Rho, T. Kozasa, W. T. Reach, J. D. Smith, L. Rudnick, T. DeLaney, J. A. Ennis, H. Gomez, and A. Tappe. Freshly Formed Dust in the Cassiopeia A Supernova Remnant as Revealed by the Spitzer Space Telescope. *Astrophys. J.*, 673:271–282, January 2008. doi: 10.1086/523835.
- [53] M. Ruderman. Crust-breaking by neutron superfluids and the VELA pulsar glitches. *Astrophys. J.*, 203:213–222, January 1976. doi: 10.1086/154069.
- [54] I.-J. Sackmann, A. I. Boothroyd, and K. E. Kraemer. Our Sun. III. Present and Future. *Astrophys. J.*, 418:457, November 1993. doi: 10.1086/173407.
- [55] D. B. Sanders, N. Z. Scoville, and P. M. Solomon. Giant molecular clouds in the Galaxy. II - Characteristics of discrete features. *Astrophys. J.*, 289:373–387, February 1985. doi: 10.1086/162897.
- [56] E. Schreier, R. Levinson, H. Gursky, E. Kellogg, H. Tananbaum, and R. Giacconi. Evidence for the Binary Nature of Centaurus X-3 from UHURU X-Ray Observations. *Astrophys. J.*, 172:L79, March 1972.

- [57] S. L. Shapiro and S. A. Teukolsky. *Black holes, white dwarfs, and neutron stars: The physics of compact objects*. 1983.
- [58] P. S. Shternin, D. G. Yakovlev, C. O. Heinke, W. C. G. Ho, and D. J. Patnaude. Cooling neutron star in the Cassiopeia A supernova remnant: evidence for superfluidity in the core. *Mon. Not. R. Astron. Soc.*, 412:L108–L112, March 2011. doi: 10.1111/j.1745-3933.2011.01015.x.
- [59] S. W. Stahler, F. H. Shu, and R. E. Taam. The evolution of protostars. II - The hydrostatic core. *Astrophys. J.*, 242:226–241, November 1980. doi: 10.1086/158459.
- [60] H. Tananbaum. Cassiopeia A. *IAU Circ.*, 7246:1–+, September 1999.
- [61] J. R. Thorstensen, R. A. Fesen, and S. van den Bergh. The Expansion Center and Dynamical Age of the Galactic Supernova Remnant Cassiopeia A. *Astrophys. J.*, 122:297–307, July 2001. doi: 10.1086/321138.
- [62] L. K. Townsley, P. S. Broos, G. P. Garmire, and J. A. Nousek. Mitigating Charge Transfer Inefficiency in the Chandra X-Ray Observatory Advanced CCD Imaging Spectrometer. *Astrophys. J.*, 534:L139–L142, May 2000. doi: 10.1086/312672.
- [63] S. van den Bergh and K. Kamper. Optical studies of Cassiopeia A. VII - Recent observations of the structure and evolution of the nebula. *Astrophys. J.*, 293:537–541, June 1985. doi: 10.1086/163259.
- [64] S. van den Bergh and K. W. Kamper. Optical studies of Cassiopeia A. VI - Observations during the period 1976-1980. *Astrophys. J.*, 268:129–133, May 1983. doi: 10.1086/160938.
- [65] J. Wilms, A. Allen, and R. McCray. On the Absorption of X-Rays in the Interstellar Medium. *Astrophys. J.*, 542:914–924, October 2000. doi: 10.1086/317016.
- [66] D. G. Yakovlev, K. P. Levenfish, and Y. A. Shibano. REVIEWS OF TOPICAL PROBLEMS: Cooling of neutron stars and superfluidity in their cores. *Physics Uspekhi*, 42:737–778, August 1999. doi: 10.1070/PU1999v042n08ABEH000556.
- [67] D. G. Yakovlev, W. C. G. Ho, P. S. Shternin, C. O. Heinke, and A. Y. Potekhin. Cooling rates of neutron stars and the young neutron star in the Cassiopeia A supernova remnant. *Mon. Not. R. Astron. Soc.*, 411:1977–1988, March 2011. doi: 10.1111/j.1365-2966.2010.17827.x.
- [68] J. L. Yun and D. P. Clemens. Star formation in small globules - Bart BOK was correct. *Astrophys. J.*, 365:L73–L76, December 1990. doi: 10.1086/185891.

- [69] V. E. Zavlin, G. G. Pavlov, and Y. A. Shibano. Model neutron star atmospheres with low magnetic fields. I. Atmospheres in radiative equilibrium. *Astron. Astrophys.*, 315:141–152, November 1996.

## COLOPHON

This document was typeset using the typographical look-and-feel classicthesis developed by André Miede. The style was inspired by Robert Bringhurst's seminal book on typography "*The Elements of Typographic Style*" and it can be found here:

<http://www.miede.de/>

---

## DECLARATION

---

I hereby declare that the work presented here is my original work. Whenever a work has been done by others, they have been acknowledged or cited properly.

*Edmonton, July 2012*

---

Khaled G. Elshamouty